Quantitative 3D microscopy reveals a genetic network predicting the local activity of anti-Aβ compounds

Daniel Kirschenbaum[1§], Fabian F. Voigt[2§], Ehsan Dadgar-Kiani[3§], Francesca Catto[1§], Chiara Trevisan[1], Oliver Bichsel[1], Hamid Shirani[4], K. Peter R. Nilsson[4], Karl Joachim Frontzek[1], Paolo Paganetti[5], Fritjof Helmchen[2], Jin Hyung Lee[3,6*+] & Adriano Aguzzi[1*+]

[1]Institute of Neuropathology, University Hospital Zurich, University of Zurich, Schmelzbergstrasse 12, CH-8091 Zurich, Switzerland

[2]Laboratory of Neural Circuit Dynamics, Brain Research Institute, University of Zurich Winterthurerstrasse 190, CH-8057 Zurich, Switzerland

Neuroscience Center Zurich, University of Zurich & ETH Zurich, Winterthurerstrasse 190, CH-8057 Zurich, Switzerland

[3]Department of Bioengineering, Stanford University, Stanford, CA 94305, USA

[4]Department of Physics, Chemistry and Biology, Division of Chemistry, Linköping University, SE-581 83 Linköping, Sweden

[5]Laboratory for Biomedical Neurosciences, Neurocenter of Southern Switzerland, Ente Cantonale Ospedaliero, CH-6807 Torricella-Taverne, Switzerland

Faculty of Biomedical Neurosciences, Università della Svizzera Italiana, CH-6900 Lugano, Switzerland

[6]Neurology and Neurological Sciences, Bioengineering, Neurosurgery, and Electrical Engineering, Stanford University

[§]Co-first authors; equal contribution

[+]Co-last authors; equal contribution

*Correspondence: adriano.aguzzi@usz.ch, ljinhy@stanford.edu

Abstract

Genetic and biochemical evidence suggests a role for amyloid-β (Aβ) in Alzheimer's disease, yet many anti-Aβ treatments are clinically ineffective. Regional heterogeneity of efficacy may contribute to these disappointing results. Here we compared the regiospecificity of various anti-Aβ treatments by combining focused electrophoretic whole-brain clearing, amyloid labelling and light-sheet imaging with whole-brain analyses of plaque topology in Aβ-overexpressing mice. Aβ plaque numbers progressed from around 1'200'000 to 2'500'000 over a 9-month period. We then assessed the regiospecific plaque clearance in mice subjected to β-secretase inhibition, amyloid intercalation by polythiophenes, and anti-Aβ antibodies. Each treatment showed unique spatiotemporal Aβ clearance signatures, with polythiophenes emerging as potent anti-Aβ compounds with promising pharmacokinetic properties and the anti-Aβ antibody showing only minor effects. By aligning (25 µm)^3 voxels that showed drug effectiveness to spatial transcriptomics atlases, we identified genes matching regiospecific Aβ clearance. As expected, *Bace1* expression was highly correlated with the regiospecific efficacy of BACE inhibition. In addition, we found that voxels cleared by polythiophenes correlated with transcripts encoding synaptic proteins, whereas voxels cleared by BACE inhibition correlated with oligodendrocyte-specific genes. The differential regional susceptibility of distinct plaque populations to specific treatments may explain the clinical failure of anti-Aβ therapies, and suggests that combinatorial regimens may improve functional outcomes.

Introduction

Different protein aggregates can target distinct microanatomical regions and give rise to distinct clinical pictures[1,2]. The boundaries of such system-specific pathologies are not always congruent with those defined by classical neuroanatomy, and their determinants are poorly understood. Likewise, most neurotropic drugs are meant to act on specific CNS regions and may be deleterious to others[3]. The above applies also to Alzheimer's disease (AD), the most prevalent neurodegenerative disease and a significant cause of disability[4]. A hallmark of AD is the deposition of amyloid-β (Aβ) plaques, and genetic evidence points to a causal role for Aβ in AD[5]. The plaque load of AD patients can be effectively reduced by quenching Aβ production[6], by reducing the propagation of Aβ aggregates[7], or by enhancing Aβ catabolism[8]. The clinical efficacy of Aβ removal is still debated[9,10], perhaps because intervention may be too late to be efficacious[11]. It is also conceivable that anti-Aβ drugs remove plaques differentially in distinct CNS regions, some of which may not coincide with the areas that matter most to proper brain functioning.

To challenge the latter hypothesis, we developed a high-throughput quantitative 3D histology (Q3D) platform for optically clarifying, staining, imaging and quantifying Aβ plaques in whole brains of mice. Aβ plaques were rapidly stained by electrophoresis, and cleared brains were imaged with a custom-built mesoscale selective plane illumination microscope (mesoSPIM)[12]. We tested the effects of the polythiophene LIN5044 which intercalates with amyloids and is therapeutic in prion diseases[13,14], the BACE1 inhibitor NB-360[15,16], and the β1-antibody[17] in APPPS1 mice[18]. We found that each drug acted onto distinct, barely overlapping brain regions. Intriguingly, the polythiophene resulted in the most potent Aβ plaque load reduction in aged mice. The alignment of whole-brain treatment maps to a spatial transcriptomics atlas allowed us to identify local transcriptional signatures correlating with the effectiveness of each drug.

Materials and Methods

Animal treatments and tissue preparation

All animal experiments were carried out in strict accordance with the Rules and Regulations for the Protection of Animal Rights (Tierschutzgesetz and Tierschutzverordnung) of the Swiss Bundesamt für Lebensmittel-sicherheit und Veterinärwesen and were preemptively approved by the Animal Welfare Committee of the Canton of Zürich (permit 040/2015). APPPS1 male and female mice were either treated with NB-360[15] BACE1-inhibitor (Novartis) orally (0.5 g inhibitor/kg chow, ~6 g chow/day/mouse = 3mg inhibitor/day/mouse), or with the β1 monoclonal IgG2a antibody recognizing the human specific EFRH tetrapeptide of amino acids 3 - 6 of Aβ[17,19] (Novartis) (0.5 mg/week, once/week in 200µl phosphate buffered saline (PBS) intraperitoneally), or with the amyloid intercalator LIN5044[13] (0.4 mg/week, once/week in 100 µl PBS). Control mice were treated with control chow, pooled recombinant non-specific IgG and PBS respectively. The ages of NB-360, β1 antibody and LIN5044 treated mice were 353 ± 21, 313 ± 9, and 308 ± 7 days, respectively (groups of old mice), as well as 61 ± 3 days, 59 ± 2 and 65 ± 2 days, respectively (groups of young mice) (Table S1) After treatments were completed mice were deeply anaesthetized with ketamine and xylazine and transcardially perfused first with ice cold phosphate-buffered saline (PBS), followed by a hydrogel monomer mixture of 4% acrylamide, 0.05% bisacrylamide and 1% paraformaldehyde[20]. Brains were harvested and were further incubated passively in the hydrogel mixture for 24 hours. The hydrogel was degassed and purged with nitrogen, followed by polymerization at 37 °C for 2.5 hours. Samples were either stored in PBS or clearing solution until Q3D clearing.

For generating the whole - brain vascular images Claudin5-GFP (Gensat.org. Tg(*Cldn5*-GFP)) mice were processed as described above.

Tissue clearing

Brains were cleared with focused electrophoretic tissue clearing (FEC) in a custom-built chamber in 8% clearing solution (8% w/w sodium dodecyl sulphate in 200 mM boric acid, pH 8.5). Standard settings were 130 mA current-clamped at a voltage limit of 60V, at 39.5 °C. Clearing time varied between 6-14 hours for a total mouse brain. The polarity of the electrodes was switched after approximately 50% of the total clearing time.

Transparency was assessed by visual inspection. The clearing solution was circulated from a buffer reservoir of 250 ml. After clearing a brain 60 ml of clearing buffer was exchanged with fresh buffer before starting to clear the next sample. Q3D-clearing chambers were 3D-printed, and clearing was done in an incubator at 39.5 °C. For details on the chamber design see supplementary material and model repository (**Figure S1**)[21].

Relative electrical resistivity measurement between brain tissue and buffer

For electrical resistivity comparison 4% paraformaldehyde fixed mouse brain in PBS, and PBS was used. Platinum electrodes (1.5 x 0.2 mm) were mounted at a distance of 2 mm and a constant voltage of 30 V was applied. Current measurements were used to calculate the resistance between the electrodes. Brain tissue resistance was measured by sticking the electrode-pair into the brain in 3 different areas (frontal cortex, occipital cortex and brainstem). In each area current values were measured three times. The resistivity in the buffer was measured nine times. These measurements resulted in a 1200 Ohm resistance in the brain and 300 Ohm resistance in the buffer. As the electrode setup and the voltages were constant for every measurement, the relative resistivity was calculated as the ratio of the two resistivity measurements, resulting in a resistivity ratio of 1:4 (buffer:brain).

Comparison between Q3D and CLARITY

Hydrogel embedded mouse brains of 3-month-old mice were either cleared with 8% clearing solution passively for 24 hours at 39°C (n = 3) or for 4 or 6 hours either with Q3D or CLARITY[22] clamped at 130 mA at 60V at 39 °C (four active clearing groups each n = 3). After clearing, brains were washed with PBS followed by refractive index matching and brains were mounted in quartz cuvettes. Samples were illuminated with a ~4-5 µm wide 647 nm laser beam, calibrated to 0.35 mW power. Each brain was illuminated stereotypically from dorsal at 10 aligned points with 0.5 mm spacing along the rostro-caudal axis with the same incumbent laser power (as measured through the imaging medium and cuvette). This was done in 3 parallel lines (one in the midline, and a line 2 mm left and right from it) resulting in 3x10 measurement points per brain (**Figure S1f**). The point pattern was defined starting from the lambdoid fossa. The transmitted light was measured at each point with a digital optical power meter (Thorlabs, PM100D, Compact Power and Energy Meter Console, Digital 4" LCD; Thorlabs S130C photodiode sensor). The mean and standard error of the mean of all points

for each sample was plotted (**Figure S1f-g**). We also plotted the mean transmitted light on every rostro-caudal level resulting in 10 datapoints summarizing the 3 parallel lines (two hemispheres and the midline) (**Figure 1c**). These 10 points per sample were submitted to a one-way ANOVA, $\alpha = 0.05$, which was corrected with Tukey's test for multiple comparisons.

Electrophoretic staining with Q3D

Histochemistry by iontophoretic tissue staining was initially done by layering paraffin and agarose around the sample in order to limit current flow to the tissue. Later, Q3D staining chambers were 3D-printed (**Figure S2a-b**). As buffer 50 mM tris, 50 mM tricine at pH 8.5 was used for electrophoresis. Tests in native polyacrylamide gel electrophoresis followed by silver staining (Thermo Scientific Pierce Silver Stain Kit, #24612) showed as expected, that electrophoretic mobility is highly pH and buffer dependent (F**igure S2d-g**). Amyloid plaques were stained with a combination of luminescent conjugated polythiophenes (LCP), heptamer-formyl thiophene acetic acid (hFTAA) and quadro-formyl thiophene acetic acid (qFTAA)[OBJ]. The combination of these dyes was used for the discrimination of neuritic[23][OBJ][OBJ] at different maturation states[22].

Refractive index matching

Brains cleared and stained with Q3D were refractive index (RI) matched to 1.46 with a modified version of the refractive index matching solution[20], by including triethanolamine (tRIMS). tRIMS was made by mixing Histodenz (Sigma #D2158)(100 mg), phosphate buffered saline (75 ml), sodium azide (10% w/v, 500 µl), tween-20 (75 µl) and triethanolamine (42 ml). tRIMS maintains RI while reducing the amount of Histodenz required and improves transparency. After prolonged air and light exposure tRIMS tends to undergo browning, however in air-tight tubes at 4 °C samples remain stable for at least two years.

Antibody and polythiophene staining

Slices from formalin fixed and paraffin embedded brain tissue from a 13-month-old APPPS1 mouse were stained for Aβ plaques. Slices were either stained with mouse anti-human $A\beta_{17-24}$ antibody (4G8, Biolegend SIG-39220) after antigen retrieval with 10% formic acid. Slices were blocked with M.O.M. Kit (BMK-2202) and the primary antibody was detected with alexa-594 conjugated goat anti-mouse IgG (Invitrogen A-11005, 1:1000 dilution). Alternatively, slices were stained with Aβ N3pE rabbit anti-human antibody (IBL 1A-018,

1:50 dilution) after 10% formic acid antigen retrieval, followed by blocking with 10% goat serum, detected with alexa-594 conjugated goat anti-rabbit IgG (Invitrogen A-11037, 1:500 dilution). Both antibody stainings were followed by staining with qFTAA (0.75 µM in PBS), hFTAA (3 µM in PBS) for 30 minutes, followed by diamidino-phenylindole (DAPI) staining. Slices were imaged with a Leica SP5 confocal microscope with a 10x air objective (numerical aperture 0.4). qFTAA and hFTAA staining was imaged by exciting both at 488 nm and collecting emission between 493 - 510 nm and 530 – 579 nm respectively. The dynamic range of images was adjusted consistently across stainings and images (3.57 µm/pixel) were median filtered with ImageJ (pixel radius 0.5).

Drug distribution measurements

NB360 was applied orally in three male C57BL/6 black mice at 5mg/kg body weight dose level at 0.5 mg/ml in water with 0.5% methylcellulose and 0.1% Tween-80. Based on preceding pharmacokinetic studies[15], one hour later brains were harvested followed by homogenization in water and acetonitrile precipitation. NB360 levels were measured with tandem mass spectrometry with electrospray ionisation. LIN5044 was administered intraperitoneally into male C57BL/6 black mice at 16 mg/kg body weight dose level at 4 mg/ml in PBS. As preceding pharmacokinetic studies were not available, two- and six-hour incubation timepoints were chosen each with three mice. Brains were homogenized in water and precipitated with methanol. LIN5044 levels were measured with high pressure liquid chromatography - tandem fluorescence detection. Brain region's drug levels were compared with one-way ANOVA, $\alpha = 0.05$, for each compound and timepoint separately (NB360, LIN5044 2 hour, LIN5044 6 hour); multiple comparisons were corrected for with Tukey's test.

Antibody brain-distribution measurements

C57BL/6 mice were injected one-time either with β1 antibody (n=6) or for control with pooled recombinant non-specific IgG (n=2) (0.5 mg in 200 µl intraperitoneally) or no injection (n=1). β1 injected mice were sacrificed 6 (n=3) or 24 hours (n=3), while control mice 24 hours after injection. Amyloid β Protein Fragment 1-42 (A9810, Sigma) was diluted at 1 µg/mL in PBS and passively absorbed on multiwell plates (SpectraPlate-384 HB, Perkin Elmer) overnight at 4 °C. Plates were washed three times in 0.1% PBS-Tween 20 (PBS-T) and blocked with 80 µl per well of 5% skim milk (Migros) in 0.1% PBS-T for 2 h at room temperature. β1-antibody

and pooled recombinant IgG were used as positive and negative controls, respectively. Blocking buffer was discarded and samples and controls were added dissolved in 1% skim milk in 0.1% PBS-T for 1 h at 37°C. 2-fold dilutions of β1-antibody, starting at a dilution of 1000 ng/ml in 1% skim milk in 0.1% PBS-T were used as calibration curve. Goat polyclonal anti-mouse antibody (1:1'000, 115-035-062, Jackson ImmunoResearch) was used to detect murine antibodies. Chromogenic reaction was induced by addition of TMB Stabilized Chromogen (SB02, Thermo Fisher Scientific) and stopped by addition of 0.5 M H_2SO_4. Absorbance was read at λ = 450 nm. Unknown β1-antibody concentrations were interpolated from the linear range of the calibration curve using linear regression (GraphPad Prism, GraphPad Software).

Whole-brain imaging

Whole brain images were recorded with a custom-made selective plane illumination microscope (mesoSPIM)[12]. SPIM imaging was done after clearing and refractive index matching. The laser/filter combinations for mesoSPIM imaging were as follows: For qFTAA at 488 nm excitation a 498 - 520 nm bandpass filter (BrightLine 509/22 HC, Semrock / AHF) was used as emission filter; for hFTAA at 488 nm excitation a 565 - 605 nm bandpass filter (585/40 BrightLine HC , Semrock / AHF) was used. Transparent whole-brains were imaged at a voxel size of 3.26 × 3.26 × 3 μm^3 (X × Y × Z). For scanning a whole brain 16 tiles per channel were imaged (8 tiles per brain hemisphere). After the acquisition of one hemisphere, the sample was rotated and the other hemisphere was then acquired. The entire process resulted in typical acquisition times of 2-3 hours, followed by stitching[24]. Data accumulated from one brain ranged around 600 GB in size. Further technical details of the mesoSPIM[12].

Computational and statistical analysis

The following computations were performed using custom scripts written in Python and R[25] as well as existing third-party libraries (Table 2). The 2-channel (498–520 nm and 565-605 nm) substacks for each brain hemisphere were first stitched together with Terastitcher[24]. The result was then downsampled from the acquired resolution (3.26 µm lateral, 3 µm depth) to an isotropic 25 µm resolution and was then registered to the Allen Institute 25 µm average anatomical template atlas[26]. This was performed automatically using a combination

of affine and b-spline transformation registrations with a mutual information similarity metric, using parameters influenced from previous studies performing mouse whole-brain fluorescence quantification[27]. The resulting pairs of transformations were used in subsequent steps to transform coordinates in the raw data space to the template atlas space (**Extended data figure 1**).

The 565-605 nm channel at its original resolution was used to determine the locations of aggregates of amyloid-β stained with qFTAA and hFTAA. A random forest classifier was used to classify each voxel as either "belonging to a plaque" or "background". This classifier was generated using the open-source Ilastik framework[28], and trained on a random subset of data (random stacks, 3 stacks [187x176x1242 pixels] picked from every experimental group) that was separately annotated by two neuropathologists. Amyloid-β aggregates were considered to be the individually connected components from this binarized volume. The three-dimensional center of mass and total volume was then calculated for each component. Connected components with a volume below a global threshold were considered noise and ignored. The remaining centers of mass were used to look up the peak fluorescent intensity of each plaque in the 498-520 nm (qFTAA) channel, and plaque maturity was calculated as the plaque's peak intensity in the 498-520 nm (qFTAA) channel divided by its peak intensity in the 565-605 nm (hFTAA) channel22 (Extended data Figure 1).

After downsampling each aggregate center to 25 µm resolution and applying the optimized registration transformation, the number of aggregates were counted at each voxel in this atlas space (**Extended data Figure 2**). Smoothed heatmaps were generated by placing a spherical ROI with 15-voxel diameter (= 375µm) at each voxel and summing the plaque counts within the ROI This ROI diameter was set to match the mean spatial jacobian determinant of the previously-registered b-spline transformation across all samples. This method for smoothing and accounting for variable registration quality has also been described in previous whole-brain studies[27]. Voxel-level statistics across treated and control brains involved running a two-sided t-test at each heatmap voxel across the two groups. Each voxel p-value was adjusted using the Benjamini-Hochberg method[29]. These adjusted p-value maps were then binarized with a threshold of 0.05 or 0.10 for subsequent analysis or visualization.

The transformed locations of each plaque were also further grouped into 134 different anatomically segmented regions in the Allen Reference Atlas[26] for further statistical analysis between longitudinal groups. Similar heatmap generation, voxel statistics, and regional statistics were performed for two other metrics: the mean plaque volume, and the mean plaque maturity intensity ratio in each 25 µm voxel.

The voxel-level statistics for each treatment group was also compared against a spatially-resolved transcriptomics database consisting of 23371 genes across 34103 locations throughout the brain[30]. Since the data from this study and the spatial transcriptomic database were both in the ARA coordinate space, it was possible to spatially compare each gene's expression map with each treatment group's binarized p-value map using a similarity metric. In this case, mutual information was used as the similarity metric since it will detect any sort of relationship between these two discrete datasets. In order to rank the relevancy of genes in contributing to the spatial map of plaque removal efficacy for a particular compound, we generated a ranked list of genes for each treatment group, sorted by their corresponding mutual information score. We additionally used the Allen Cell Types Database to assign each gene to its most likely cell type (astrocyte, microglia, neuron, oligodendroglia, mixture)[31].

Key Resources are summarized in supplemental table 2 (**Table S2**). *See also References*[32-35]

Results

Rapid tissue clearing and staining platform

Detergent-mediated lipid extraction from hydrogel-embedded tissues is facilitated by electrophoretic mobilization of detergent molecules[22,36] in a buffer-filled container. However, the current traversing 4% paraformaldehyde-fixed PBS-soaked brain tissue is 4-fold lower than that of PBS (**Figure S1g**), Therefore, electrophoresis becomes short-circuited by the buffer surrounding the specimen. We resolved this issue by designing a focused electrophoretic clearing (FEC) device that uncouples buffer recirculation in the anodic and cathodic circuits with an insulating layer (**Figure 1a and S1**). By forcing the electrical current to traverse the tissue specimen (130 mA in constant-current, 39.5 °C), FEC reduced the clearing time from 48-120 with CLARITY to 6-14 hours [22,36] (**Figure 1b-d and S1g**).

For Aβ plaque staining of intact mouse brains by electrophoresis, we designed two symmetric plastic chambers containing electrophoretic buffer and an electrode. The inner faces of the chambers were cast with 10% polyacrylamide in tris-tricine buffer and functioned as electrically conductive contact surfaces. The sample was mounted with a holder between the two acrylamide walls. This allowed electrophoresis to occur through the buffers, the gels and the tissue specimen; spanning 10 cm between the two electrodes (**Figure S2a-b**). The electric resistance of the electrophoretic system (20 V, 20 °C) increased from initially ~2 kΩ to ~20 kΩ after 2 hours (**Figure S2c**).

Figure 1. Focused electrophoresis improves tissue clearing efficiency. (a) Schematics of focused electrophoretic clearing (FEC). An insulating layer (striped pattern) constrains the electrical field through the tissue. (**b**) Comparison of mouse brains cleared by FEC (6 hrs) and passive (3 days)(after index-matching). Passive clearing was incomplete even after 3 days. (**c**) Light transmittance of tissue increased more rapidly with FEC than with CLARITY. Each group consists of 3 brains, and each brain was measured in 30 points (0.35mW input power, 647nm wavelength). The first point was measured through the lambdoid fossa. From there the laser beam was moved 0.5 mm in the midline rostrally for the next measurement. This was repeated concluding in 10 measurement points along an imaginary line in the midline spanning 5 mm. Additional 20 points were measured in a similar fashion just with 2 mm lateral (left and right from the midline) displacement defining coronal planes. Black circles: each point is the mean from three transmittance readings from points next to each other on the neighboring imaginary lines defining a coronal plane (resulting in 10 datapoints plotted per brain; per group [n=3] 30 points plotted). (One-way ANOVA *** $p<0.001$, **** $p<0.0001$). (**d**) The brain vasculature of Claudin5-GFP mice after 14 hours of clearing was imaged sagittaly by mesoSPIM. Digital reslicing and visualization by maximum-intensity projection demonstrates that focused clearing resulted in highly uniform signals. Darkened areas are due to stitching/vignetting artifacts.

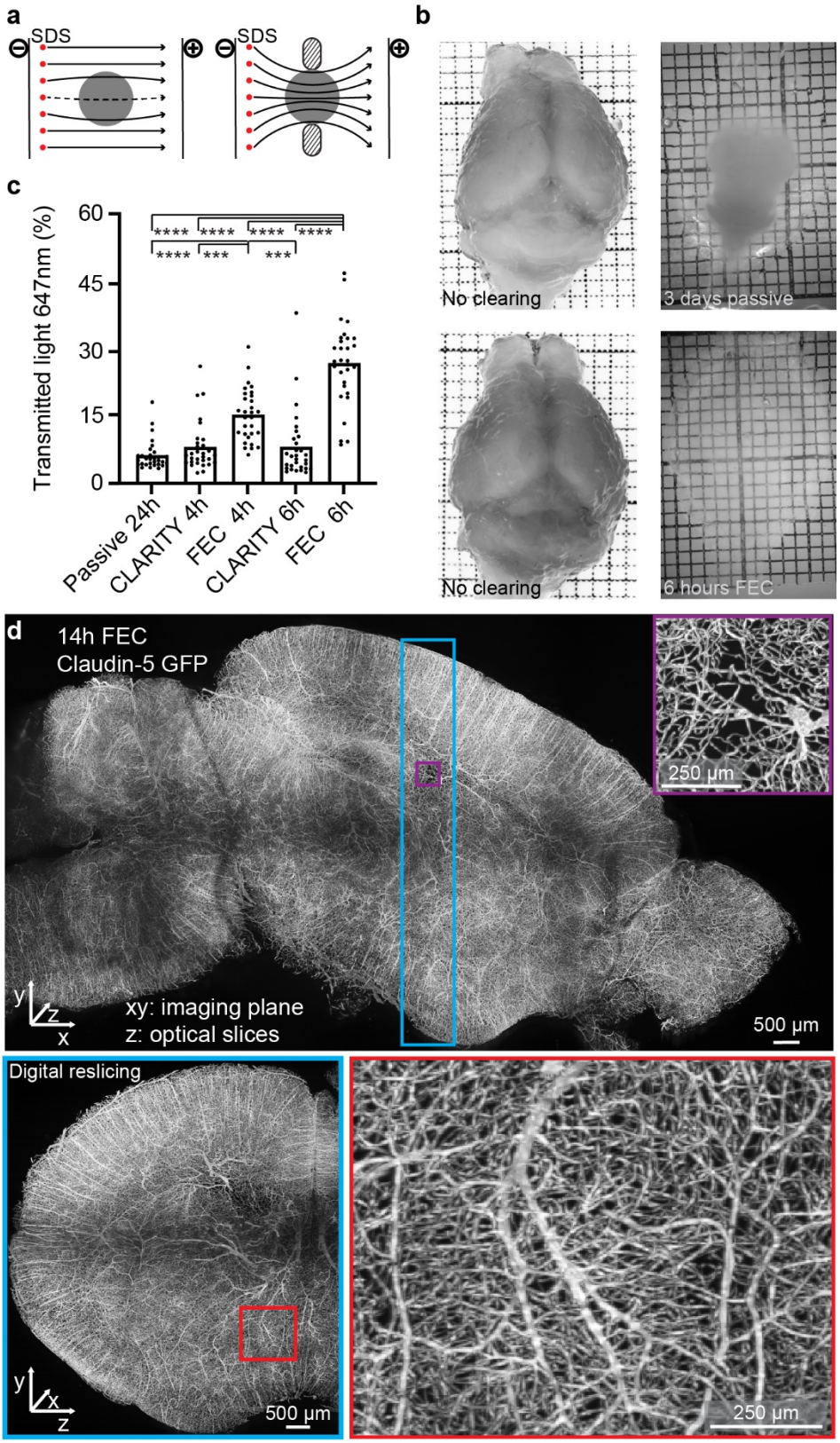

Figure 1

We then ran native-gel electrophoreses of proteins with various charges at different pH and ionic strengths. Tris-tricine (50 mM each) at pH 8.5 yielded the best results (**Figure S2d-g**). As expected, the electrophoretic mobility of proteins was influenced by the charge of covalently coupled fluorophores (**Figure S2d-g**). The polythiophenes qFTAA (616.5 g/mol, m/z = 205.5) and hFTAA (948.9 g/mol, m/z = 237.125) were dissolved in agarose (600 µl, congealing temperature 26-30 °C) and cast on the acrylamide-tissue interface in order to confine them to the smallest possible volume. Under these conditions, the dye front traversed the entire brain within 2 hours. `

An uneven passage of the dye front through the brain may lead to local inhomogeneities of plaque detection, particularly at gel-liquid interfaces. To investigate this question, a hydrogel-embedded and cleared APPPS1 brain was electrophoretically stained with polythiophenes (2 hours) and cut into 500-µm sagittal sections with a vibratome. Free-floating sections were imaged with a fluorescent stereomicroscope. Then, the sections were passively re-stained with the same polythiophene dyes using a well-established protocol[23,37] and images were acquired again. The numbers of Aβ plaques were 3085 and 3061 plaques before and after re-staining, respectively, and their morphology was indistinguishable (**Figure 2a**). Hence the sensitivity and spatial homogeneity of electrophoretic plaque staining of whole brains was not inferior to that of conventional histochemical slice staining.

Figure 2. Homogeneous whole-brain Aβ plaque stain by electrophoretic infusion of qFTAA and hFTAA polythiophenes. (a) After whole-brain electrophoretic staining ("Q3D stain") with qFTAA and hFTAA, sagittal slices (500 µm) were cut and plaques were counted. No additional plaques were stained when the same slice was re-stained passively with the same dyes ("Q3D + passive"). Slight differences between the two images are due to focal shifts after the slices were processed and reimaged. (**b**) Plaque maturation states determined with qFTAA vs hFTAA were compared to those identified by N3pe (pyroglutamylated Aβ) vs $Aβ_{17-24}$ (all Aβ moieties). APPPS1 brain sections (paraffin, 10 µm) were stained with Aβ-N3pE or $Aβ_{17-24}$ and subsequently co-stained with qFTAA and hFTAA. Aβ-N3pE detected plaques similarly to qFTAA, while hFTAA highlighted additional plaques (white arrowheads). Conversely, $Aβ_{17-24}$ labeled the entire plaque population similarly to hFTAA (white arrowheads). (**c**) Lightsheet imaging and digital reslicing of cleared whole brains. Plaques were visible in the cortex and in deep diencephalic areas, indicative of homogeneous dye penetration and image acquisition. Coronal and horizontal reslices showed only minimal axial anisotropy. Plaque maturity was assessed in by qFTAA-hFTAA co-staining. In an exemplary image, hFTAA identified all plaques (blue arrows) whereas qFTAA stained the cores (white arrows) of a subpopulation of more mature plaques. (**d**) Whole brain hemisphere rendering of an APPPS1 mouse with hFTAA signal. The cerebellum, in which the Thy1 promoter is inactive, was unaffected.

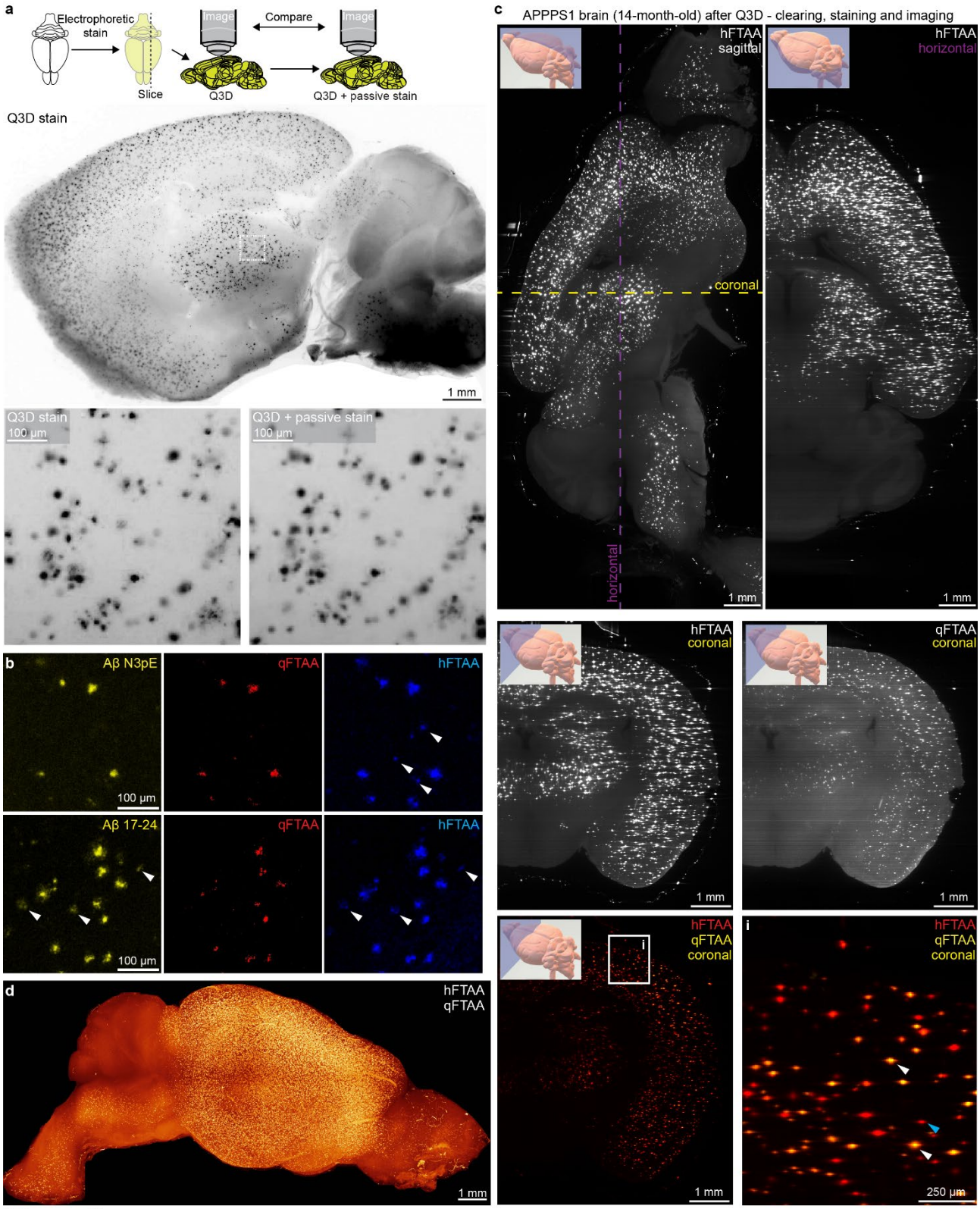

Figure 2

Aβ plaques undergo a maturation process that can be visualized by state-specific antibodies: Aβ17-24 recognizes early maturation states and stains the entire plaque surfaces, whereas N3pE labels modified forms of Aβ which accumulate at later stages[38]. Likewise, the polythiophene qFTAA stains the cores of plaques in older mice, whereas hFTAA stains the entire area of early plaques, and was shown that the qFTAA/hFTAA ratio represents plaque maturity[23]. We therefore asked if polythiophenes can report maturation states in amyloid plaques. Histological sections (3 µm) from paraffin-embedded APPPS1 brains were stained with Aβ17-24 or N3pE, followed by staining with qFTAA and hFTAA. hFTAA and Aβ17-24 antibody stained the entire plaques throughout the slice, whereas qFTAA and N3pE stained the cores of a subset of plaques (**Figure 2b-c**). Some Aβ17-24 positive but N3pE negative plaques were detectable with hFTAA but not with qFTAA, suggesting that these contained less mature amyloid. We aimed to combine this Q3D approach, comprising focused electrophoretic clearing and plaque staining, with whole-brain imaging and quantitative 3D analysis to investigate the regiospecific efficacy of various anti-Abeta compounds in reducing plaque load.

Evaluation of anti-Aβ therapies by Q3D

Groups of 2-month old or 11-month old APPPS1 mice (30 and 25 mice/group, respectively) were treated for 90 days (until 5-, and 14-months of age, henceforth referred to as “young” and “old”, respectively) with the BACE1 inhibitor NB360 via food chow (0.5 g inhibitor/kg chow, ~3 mg inhibitor/day/mouse), with β1 antibody against Aβ (0.5 mg in 200µl PBS 1x/week intraperitoneally), or with the amyloid-binding compound LIN5044 (0.4 mg in 100µl PBS 1x/week intraperitoneally) (**Table 1**). Control treatments included control food chow and intraperitoneally injected recombinant pooled IgG or PBS, respectively (**Figure 3a**).

Mice were sacrificed one week after the last treatment, and brains were subjected to the complete Q3D pipeline (clearing, staining, imaging and quantification). Raw data volumes were transformed to the coordinate space of the Allen Brain Atlas[26] and anatomically registered. We then performed automated plaque segmentation and regional quantification of plaque pathology (**Figure 3, Figure 4a, Extended data figures 1-2, Table S3**). The 40 brain regions of one hemisphere displaying the most significant treatment effect were plotted for plaque count, mean size and maturity (qFTAA/hFTAA ratio).

Figure 3. Data representations indicate differences between brains of control and treatment cohorts. **(a)** APPPS1 mice were treated with antibodies, the BACE1 inhibitor NB360, the polythiophene LIN5044 or appropriate controls. (**b**) Heatmaps of mean plaque densities and sizes are shown across all the treatment and control groups. For each cohort an optical brain slice from lightsheet data is shown (Raw data). Plaque loads in aged mice are much higher than in young mice. The BACE1 inhibitor NB360 treatment suggests reduced plaque counts in 5 – month – old mice. LIN5044 treatment suggests decreased mean plaque size in 14 – month – old mice. In some cases the optical brain slices do not precisely represent the anatomy of the atlas-registered heatmap-slices. This is because the mounting (and thus the orientation) of the brains in the microscope is variable.

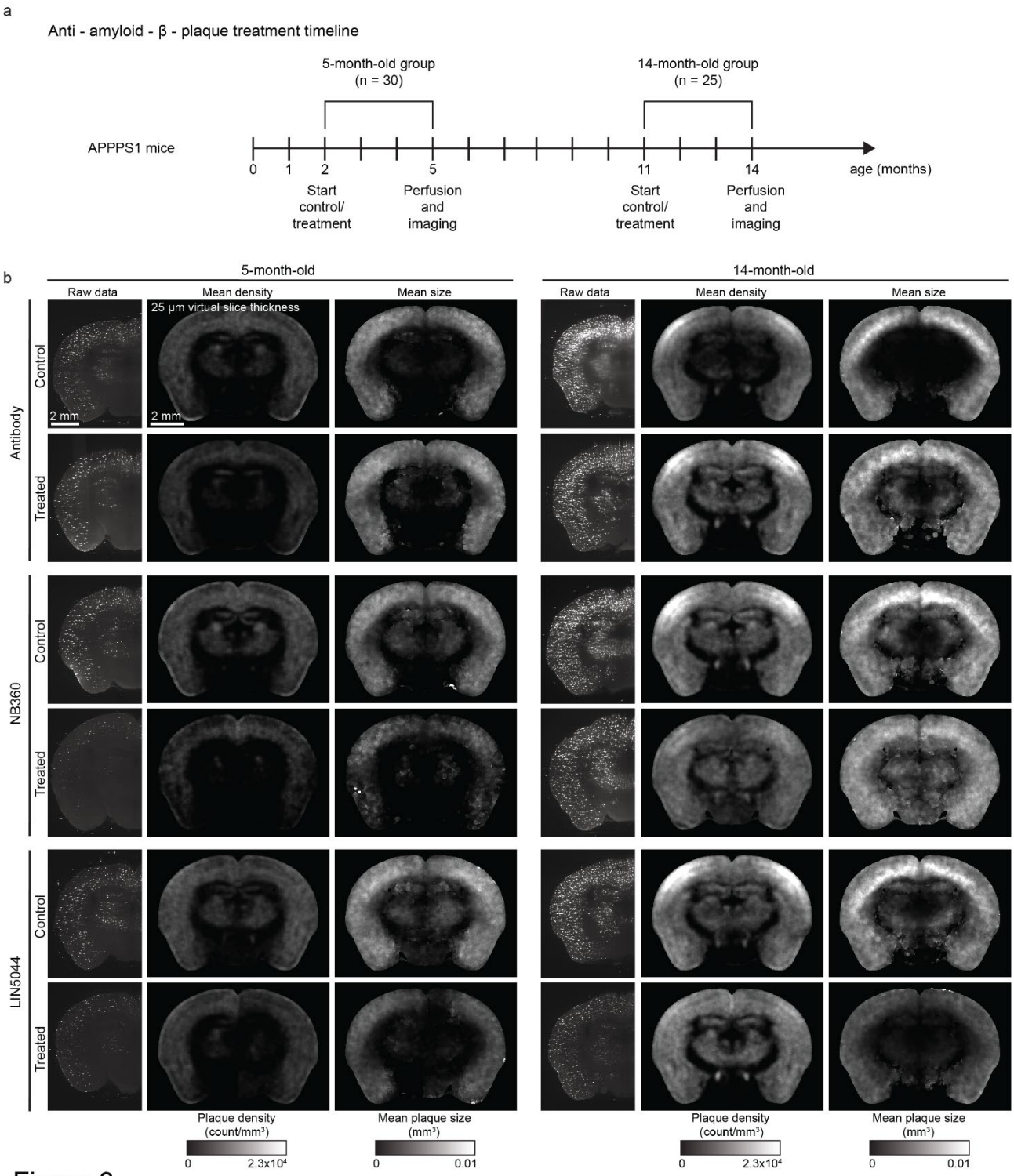

Figure 3

Voxel-level plaque counts, mean size, and maturity were determined for each treatment group (**Extended data figure 2a-c, Table 1**). Corresponding voxels of brains treated with anti-Aβ compounds and their respective controls were individually compared by inferential statistics (**Extended data figure 2d**). This allowed us

to identify "Significantly Altered Voxels" (SAV) at various levels of statistical stringency across entire brain volumes. SAV heatmaps were digitally resliced into coronal and sagittal sections.

Correlation of local efficacy with neuroanatomical areas

The effects of the β1 antibody were surprisingly small. In young mice, plaque density was slightly decreased (gustatory areas and claustrum: p = 0.014) whereas size was marginally increased (claustrum: p = 0.044), and plaque maturity was unaffected. In old mice there was no effect (**Extended data figure 3-4, Figure S3-4**). In contrast, NB360 reduced robustly plaque density and, to lesser extent, plaque size in 5-month-old mice. The plaque density reduction was most pronounced in subcortical areas (claustrum: p = 0.004) and in ventral and posterior cortical areas including the perirhinal and posterolateral visual area (both p = 0.004). Plaque size reduction was particularly strong in the amygdala and piriform area (both p = 0.024) (**Figure 4-5, Extended data figure 5-6**). Plaque maturity (based on the qFTAA/hFTAA fluorescent ratio) was increased in superficial cortical areas (e.g. olfactory areas p = 0.011) but decreased in deep subcortical structures (e.g. amygdala p = 0.017) (**Figure 4b, d and S5**). In old mice, NB360 had no significant effect on plaque density, size and maturity (**Figure 4, Extended data figure 5-6, S5**).

Figure 4. Region and age-specific plaque clearing by various anti-Aβ treatments. (**a**) After every brain was registered to a reference atlas, plaques were grouped by anatomical brain regions. The mean plaque density, size and maturity was compared between control and treated brains for corresponding brain regions. These statistical tests resulted in heatmaps of significance by anatomical brain regions. (**b**) NB360 reduced plaque density and size in brain regions in 5-month but not in 14-month old-mice. Plaque-core maturity was increased in cortex but decreased in subcortical structures. LIN5044 was effective on cortical areas, but only at 14 months. (**c-d**) Histograms visualizing the changes in plaque size and maturity upon different treatments. (**c**) NB360 did not reduce the size of plaques in aged mice. NB360 and LIN5044 reduced the prevalence of large plaques in young mice, and LIN5044 reduced it also in old mice. (**d**) NB360 affected the plaque maturity of young but not of old mice. Isoctx – isocortex, OLF – olfactory areas, HPF – hippocampal formation, CTX sp – cortical subplate, CNU – caudate nucleus, TH – thalamus, HY – hypothalamus, MB – midbrain, HB – hindbrain, CB – cerebellum

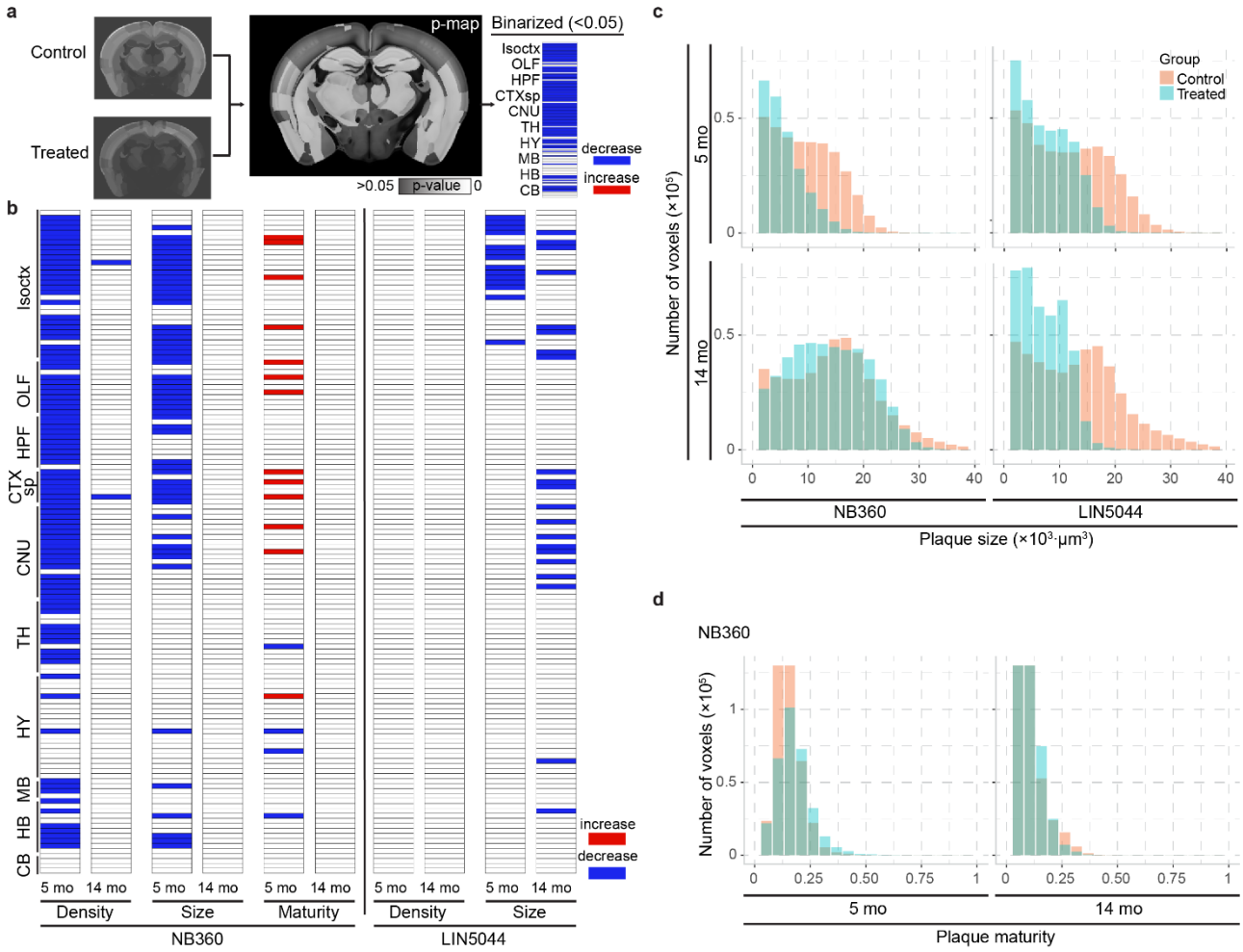

Figure 4

LIN5044 reduced conspicuously plaque sizes, but only marginally plaque density, in old mice (**Figure 3-4, Extended data figure 7-8**). Plaque sizes were preferentially reduced in subcortical areas (medial septal complex and amygdala: p = 0.0048 and 0.012 respectively) and cortical areas with a rostro-dorsal emphasis (supplemental somatosensory area: p = 0.0067). The effect of LIN5044 on mean plaque size was more pronounced in old mice, but the spatial distribution of the treatment effect was similar in young and old mice, notably including the auditory and somatosensory cortex (p = 0.0197 and p = 0.0277 respectively) (**Figure 4, Extended data figure 8**). In contrast, plaque density reduction in young mice was less conspicuous (**Figure 4, Extended data figure 7**).

Regional drug – effect analysis based on voxel-level probability distribution

The analyses above assumed that the boundaries of treatment effectiveness coincide with neuroanatomically defined regions, which might not be the case. We therefore decomposed atlas-registered brains into spatially registered voxels (25 x 25 x 25 µm). We quantified plaque density, size and maturity within each voxel, and generated descriptive statistics for each treatment cohort (**Figure 3, Extended data figure 2**). Next, we tested for significant treatment effects between corresponding voxels for treated and respective control cohorts (**Figure 5a-b, Extended data figure 1-2**). We found that neuroanatomical assignment of treatment effectiveness failed to capture conspicuous peaks of regiospecific therapeutic efficacy, and that it overestimated the volume of treatment-affected brain tissue (**Figure 5c, Extended data figure 9e**). Voxel-level heatmaps of p-values showed that BACE1 inhibition reduced plaque counts most effectively in the posterior and ventral telencephalon (**Figure 5a, Extended data figure 5**), whereas LIN5044 reduced the size of plaques primarily in rostro-dorsal areas (**Figure 5a, Extended data figure 8**). These effects were largely symmetric across the midline and showed sharp boundaries lining the deep cortical layers (LIN5044), the thalamus, and CA3 (NB360) (**Extended data figure 5-8**). The β1-treated young mice showed a patchy plaque count reduction in the brainstem (**Figure 5b, Extended data figure 4**). However, these effects were marginal and therefore β1 was excluded from further analyses.

The inferred effects of NB360 and LIN5044 rely on complex computations on terabyte-sized datasets. To intuitively visualize these effects, we randomly selected single cortical mesoSPIM images of atlas-registered brains from each treatment and control groups. Upon segmentation, we color-coded plaques based on their size. **Figure 5a** and **Extended data figure 9** confirm the plaque density and plaque size reduction in NB360 treated young mice and LIN5044 treated old mice, respectively.

Since LIN5044 and NB360 differ in their vehicle, route and schedule of administration, the different application modes may contribute to the patterns distinguishing LIN5044 and NB360. To test for this possibility, we repeated the computations by testing LIN5044-treated mice against the NB360 control group, and vice versa. The patterns remained stable even under these conditions (**Figure S6-7**). Conversely, testing the control groups against each other did not reveal any significant treatment patterns (**Figure S8a**).

Male and female mice did not differ in plaque burden (**Figure S8b**).

Colocalization analysis reveals little overlap in the regiospecificity of therapies

As a global measure of regiospecific similarity, we counted the overlapping SAVs in each treatment pairs and metrics (plaque density, mean plaque size and maturity) (**Table 2**). The maximal SAV overlap between pairs was <1% or <2.65% ($p<0.05$ or $p<0.1$, respectively) indicating that each treatment had a unique regiospecific fingerprint (**Figure 5d-e, Table 2**). Hypergeometric tests confirmed that overlaps were not significant ($p<0.03$).

The LIN5044 and NB360 SAVs appeared to cluster in distinct patterns (**Figure 5d, Supplemental video 1**). To probe the randomness of such clusters, we measured the number of connected components (neighboring SAVs that are touching each other) in NB360 and LIN5044 treated brains (13710 and 18553, respectively).

Figure 5. Voxel-based analysis of the brain shows regional and temporally distinct anti Aβ treatment effects. (**a**) We generated 3-dimensional maps of SAVs (representative slices, $0.05<p<0.1$ blue, $p<0.05$ red. reference atlas grey). Each map summarizes all the treated and control samples within a cohort (8-12 samples). These maps identified fingerprints of regiospecific efficacy unique to each treatment modality. NB360 unfolded its strongest effect on plaque counts and size of young mice in postero-ventral areas, but not in aged mice. LIN5044 showed a profoundly divergent regiospecificity with antero-dorsal peaks in aged mice, and targeted primarily the size of plaques. The plaque number and size reduction suggested by the voxel maps was confirmed by looking at randomly picked cortical (white inserts on heatmaps) optical slices (Optical slice), color-coded by plaque size. (**b**) β1 treatment SAVs (plaque counts) in the brainstem. (**c**) Seeking an unbiased volume unit for spatial analysis we divided brain data into spherical voxels (ø 750 µm). Reference atlas based anatomical normalization overestimates the volume of treatment-affected brain compared to voxel-level analysis. (**d-e**) Comparing the strongest treatment effects shows that SAVs for plaque size reduction by LIN5044 in 14-month-old mice and NB360 in 5-month-old mice cluster separately with limited spatial overlap (*p = 0.03, hypergeometric test). (**f**) To validate that these treatments create non-random SAV clusters Monte-Carlo simulations were run (500 simulations randomly distributing the experimentally measured number of voxels), and the number of connected components was counted. LIN5044 and NB360 SAVs show at least 5-fold higher clustering than random.

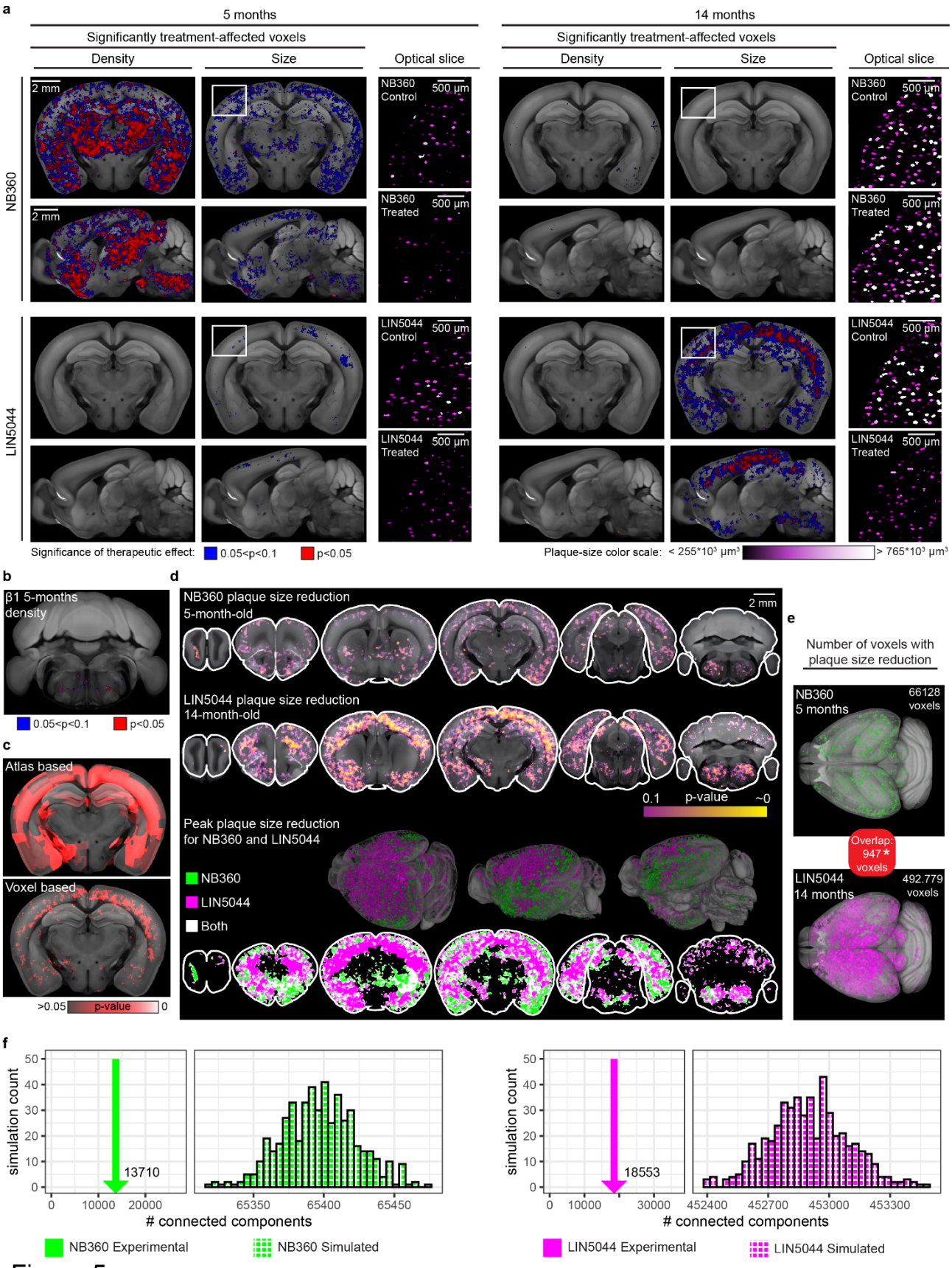

Figure 5

We then generated 500 Monte Carlo simulations with the same number of SAVs than we measured experimentally, but without constraints on their spatial distribution. We found that the number of connected components in the experimental measurements was at least 5-fold lower than in the simulations, indicating that the SAVs are grouped into distinct, spatially confined clusters (**Figure 5f**).

Regiospecificity is not due to pharmacokinetic differences

To test if the regiospecificity was caused by differential penetration of therapeutic compounds, we tested the biodistribution of β1, NB360 and LIN5044 by dissecting brains into 8 standard regions (**Extended data figure 10a**). NB360 levels were measured 1 hour after oral administration[15]. Since antibodies have long half-lifes[39] and limited blood-brain barrier penetration, brain levels were measured 6 and 24 hours after intraperitoneal injection. As the pharmacokinetic properties of LIN5044 are unknown, we measured brain levels 2 and 6 hours after intraperitoneal administration. LIN5044-treated brains showed higher levels in the brainstem and cerebellum ($p<0.034$ and 0.024, respectively) after 2 hours, but its distribution became homogeneous after 6 hours (**Extended data figure 10b-d**). β1 showed higher levels in the brainstem after 6, and in the brainstem and the cerebellum after 24 hours (**Extended data figure 10e, f**). However, there was no difference in antibody levels between diencephalic and telencephalic regions. Pooled non-specific recombinant IgG was used for control and did not accumulate in any brain region at 24 hours (**Extended data figure 10g**). Hence regional pharmacokinetic differences do not explain the region-specific drug effects.

Genetic networks revealed by aligning the Q3D output to gene-expression atlases of the brain

The findings above suggested that the local heterogeneity of drug efficacy may be controlled by intrinsic properties of the host brain, some of which may be genetically specified. We therefore compared the plaque-size SAVs of NB360 and LIN5044 to a gene-expression atlas reporting whole-genome expression at >30'000 spots of the mouse brain[30]. We calculated the mutual information (MI) as a similarity metric describing the interdependence of two random variables. Unlike the correlation coefficient, the MI incorporates non-linear relationships. As expected, the vast majority of genes showed low MI scores with either treatment (**Figure 6a**). However, the MI of *Thy1* was high in both treatment arms, indicating that its expression patterns was highly correlated to the spatial patterns of treatment effects (MI LIN5044 8.06×10^{-4}; NB360 5.32×10^{-4}). The

MI of *Thy1* ranked at the 99th percentile of 23371 genes for both LIN5044 and NB360. This result confirmed the validity of coupling Q3D to spatial transcriptomics data, since the APPPS1 transgene is transcriptionally controlled by the *Thy1* promoter, and anti-Aβ therapies would be logically expected to show efficacy at sites of Aβ expression. We conclude that the analysis of MI scores yields plausible and robust results that point to genetic networks controlling the efficacy of therapeutic regimens.

A second transcript showing a very strong MI score with NB360 (2.22×10^{-4}) was *Bace1*, ranking at the 96th percentile. However, the MI score of *Bace1* with LIN5044 was much weaker (1.37×10^{-4}) and ranked only at the 81st percentile. Since *Bace1* encodes the enzyme targeted specifically by NB360, the observation that its expression pattern correlated selectively with the effectiveness of NB360 but not of LIN5044 yielded a second, independent confirmation of the validity of our analysis.

Intriguingly, the effect of LIN5044 showed a high MI (7.23×10^{-4}, 98th percentile) with the spatial distribution of cx3cl1, a microglial chemoattractant mostly expressed by neurons[40] (NB360, cx3cl1 MI: 1.95×10^{-4}, 95th percentile). LIN5044 showed overall higher MI values than NB360 (**Figure 6a**). This is in line with the spatially more circumscribed LIN5044 SAV clusters compared to NB360 (**Figure 5a, c**). The genes with the highest MI score included broad neuronal and oligodendroglial markers, like *Nrgn, Snap25, Mbp* or *Plp1* (**Figure 6b**). Next, we grouped the genes ranking above the 95th percentile in MI according to cell types based on a published database[31]. This showed that the genes showing high MI with LIN5044 or NB360 associated with all cell types in the database (neurons, microglia, oligodendroglia, astrocytes). However, the genes with the highest MI were either more oligodendroglia- or neuron-associated, for BACE1 inhibition and amyloid inter-

Figure 6. Genetic networks predicting local drug responsiveness. (**a**) Mutual information (MI) between the spatial distributions of SAV and gene expression ranked cumulatively by MI (23371 genes). Dashed line: genes above the 95th percentile of MI. (**b**) Normalized MI of genes above the 95th percentile (ranked by MI, [n=1169]) for either NB360 or LIN5044. (**c**) Same raw data as in (b), but showing only the genes above the 95th percentile. Genes were color-coded according to the cell types in which they are enriched. NB360 and LIN5044 treatments were associated with oligodendroglial and neuronal genetic networks, respectively. (**d**) After genes were associated to cell-types, we ranked the genes by MI. This shows that the genes with the highest MI are overtly oligodendrocyte-associated for BACE1 inhibition, while for LIN5044 neuron-associated genes are the most frequent with high MI.

calation (LIN5044), respectively (**Figure 6c-d**). For example, the effect of BACE1 inhibition showed the strongest correlation with oligodendrocytic genes like *Plp1* or *Mbp*, while amyloid intercalation showed this with the neuronal genes *Nrgn* and *Camk2n1*.

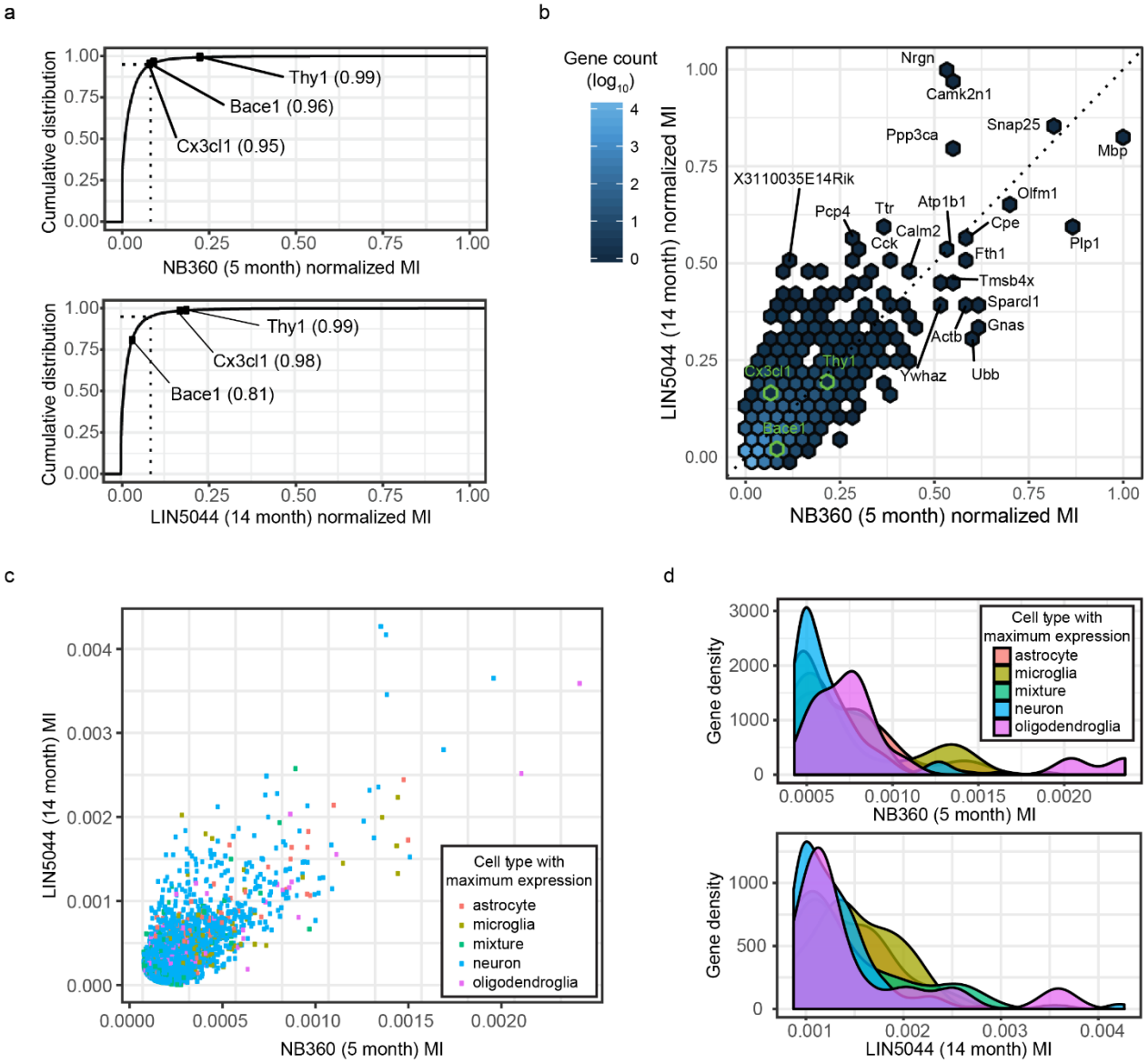

Figure 6

Discussion

Current hydrogel-based methods of whole-brain clearing are slow and often inhomogeneous. We have solved these limitations by insulating the anodic from the cathodic detergent reservoir, thereby constraining the lipid-clearing ion flow through the sample. This design enabled whole-brain clearing within ≤14 hours[22,36,41], and electrophoresis of qFTAA/hFTAA resulted in homogenous plaque staining within 2 hours. Comparison of the Q3D pipeline-including light-sheet acquisition (3.26 x 3.26 x 6.5 µm resolution) with conventional staining of histological sections showed that Q3D reliably visualizes Aβ plaques within mouse brains. Thus, we concluded that Q3D uncovers all Aβ plaques within a mouse brain. The precision of Q3D resulted in highly consistent plaque counts among age-matched APPPS1 mice (standard deviation: 2.5-3.3%). The β1 antibody showed only marginal effects in young APPPS1 mice and no effect in old mice, adding to the reports of its inconsistent efficacy in vivo[19,42]. BACE1 inhibition reduced the number and, to a lesser extent, the size of plaques in young mice but not in older mice, suggesting that it might be most effective in the prodromal stages of AD. LIN5044, a blood-brain-barrier permeable polythiophene with anti-prion activity[13,14], proved to be a potent Aβ-clearing agent. However, the regiospecific activities of LIN5044 and NB360 were almost mutually exclusive. LIN5044 was most active against rostro-dorsal amyloid deposits whereas NB360 was most effective in the ventrocaudal cortex. Moreover, LIN5044 reduced the size of plaques rather than their number, and was more active in aged mice than in young mice.

The β1 antibody showed patches of plaque count reduction in the brainstem of young mice, where higher drug concentrations were measured. This suggest that β1 might be therapeutic in young mice at higher doses. LIN5044 unfolded its effect mostly in areas perfused by the middle cerebral artery, whereas NB360 was most active in areas irrigated by the posterior cerebral artery. However, drug distribution measurements did not uncover any differences in regional bioavailability. Hence pharmacokinetic differences are unlikely to account for the regiospecific effects of LIN5044 and NB360.

The regiospecific activities of NB360 and LIN5044 may relate to their differential effects on primary and secondary nucleation [43]. In primary nucleation, monomeric Aβ coalesces into seeds. This process is dependent on the local Aβ concentration[44,45] and is highly sensitive to BACE1 inhibition[46,47]. Secondary nucleation[48], during which amyloid monomers are incorporated into preexisting aggregates, may become more important in

aged mice. Accordingly, BACE1 inhibition was more effective in deep striatal and thalamic areas where plaques become prominent at 3-5 months of age[18]. Conversely, LIN5044 is likely to affect secondary nucleation by stabilizing amyloid fibrils and decreasing their templating potential[13,14]. Since secondary nucleation depends on the concentration of seeds, it is expected to correlate with age. Accordingly, LIN5044 appears to be most potent in aged mice. Also, amyloid in APPPS1 mice is most abundant in fronto-cortical areas, which overlap with the regions of highest LIN5044 potency. Furthermore, LIN5044 is likely to inhibit the additive growth of plaques, which is congruent with its potent effect on plaque sizes rather than plaque numbers. After 3 months of treatment the number of large plaques drastically decreased whereas smaller plaques became more numerous (**Figure 4c**). This suggests that these plaques fail to grow after initiation.

Plaque burden reduction showed steep ventrocaudal (NB360) and dorsorostral (LIN5044) gradients whose boundaries did not correspond to defined neuroanatomical areas. This suggests that the regiospecificity of anti-Aβ drugs is controlled by factors other than neurophysiological or vascular territories. We therefore aligned SAV to a spatial transcriptomic atlas[30]. We identified a strong correlation between *Bace1* expression and the regiospecific efficacy of NB360, but not of LIN5044, whereas *Thy1* expression correlated with both treatments. This finding validates our unsupervised mining approach, since *Bace1* encodes the enzyme targeted by NB360, and the *Thy1* promoter drives the Aβ-producing transgene in APPPS1 mice.

This analysis revealed that the plaque clearing by LIN5044 vs. NB360 was predicted by local expression of distinct genetic ensembles. For example, the regional efficacy of LIN5044 was strongly correlated with CX3CL1, a neuron-borne microglial chemoattractant[49]. The regional variation of CX3CL1 expression may result in differential recruitment of microglia, thereby contributing to the clearance of LIN5044-intercalated amyloid. Its cognate microglial receptor CX3CR1 is highly expressed at late Aβ stages[50], which may explain the potency of LIN5044 in old mice.

NB360 effectiveness was predicted by the expression of oligodendroglial genes, whereas LIN5044 correlated with neuronal constituents. BACE1 is required for proper functioning of oligodendrocytes and myelination[51]. Intriguingly, oligodendrocyte-specific gene modules show brain-region-dependent alterations in early stages of cerebral amyloidosis, similarly to our observations of plaque reduction by NB360 in young mice[50]. This suggests that BACE1 functions as a hub orchestrating the function of oligodendrocytes and Aβ processing.

The regiospecificity of anti-Aβ therapies may be functionally relevant. The ventrocaudal effects of NB360 may modulate hippocampal and limbic functions whereas the rostro-cortical clearance by LIN5044 might act on cognitive functions[52]. Since LIN5044 and NB360 affect mostly non-overlapping areas of the brain, combination regimens may synergistically protect larger brain volumes from amyloid deposition. Notably, the computational methods developed for Aβ amyloid quantitation can enhance the statistical power of in vivo assessment of anti-Aβ drugs, and can be adapted to a broad range of protein aggregation diseases.

Acknowledgements

AA is the recipient of an Advanced Grant of the European Research Council and grants from the Swiss National Research Foundation, the Gelu Foundation, the Nomis Foundation, the Swiss Personalized Health Network (SPHN, 2017DRI17), the USZ Foundation and a donation from the estate of Dr. Hans Salvisberg. KPRN is the recipient of a Consolidator Grant from the Swedish Research Council (Grant 2016-00748). FH is a recipient of an Advanced Grant of the European Research Council (BRAINCOMPATH, project no. 670757). We thank Dr. Giulia Miracca, Dr. Todd E Golde and Dr. Soyon Hong for critical reading of the manuscript, Dr. Ulf Neumann for providing NB360 and β1, and Dr. Michael B. Smith for help with designing 3D-printed parts. Scientific sketches were used from SciDraw.io doi.org/10.5281/zenodo.3925971, doi.org/10.5281/zenodo.3925911, doi.org/10.5281/zenodo.3926119.

Authors contributions

D.K., J.H.L. and A.A. designed the study. D.K. conducted the experiments, acquired and analyzed the data. D.K. and A.A. prepared the figures and wrote the paper. F.F.V. designed and built the imaging platform. E.D.K. developed the computational analysis pipeline, analyzed data, and created figures. F.C. conducted animal experiments and imaging. O.B. worked on tissue clearing. P.N. and H.S. developed polythiophenes. K.J.F. measured antibody concentrations with ELISA. P.P. developed anti-amyloid β antibodies. F.H. helped develop the imaging platform. J.H.L. and A.A. supervised personnel and wrote the paper.

Competing Interests

J.H.L. is a founder, consultant, and shareholder of LVIS. The University of Zurich has filed a patent protecting certain aspects of the rapid-clarification technology described here.

Literature

1 Lau, A. *et al.* alpha-Synuclein strains target distinct brain regions and cell types. *Nat Neurosci* **23**, 21-31, doi:10.1038/s41593-019-0541-x (2020).

2 Shahnawaz, M. *et al.* Discriminating alpha-synuclein strains in Parkinson's disease and multiple system atrophy. *Nature* **578**, 273-277, doi:10.1038/s41586-020-1984-7 (2020).

3 Bastide, M. F. *et al.* Pathophysiology of L-dopa-induced motor and non-motor complications in Parkinson's disease. *Prog Neurobiol* **132**, 96-168, doi:10.1016/j.pneurobio.2015.07.002 (2015).

4 Fiest, K. M. *et al.* The Prevalence and Incidence of Dementia Due to Alzheimer's Disease: a Systematic Review and Meta-Analysis. *The Canadian journal of neurological sciences. Le journal canadien des sciences neurologiques* **43 Suppl 1**, S51-82, doi:10.1017/cjn.2016.36 (2016).

5 Hardy, J. & Selkoe, D. J. The amyloid hypothesis of Alzheimer's disease: progress and problems on the road to therapeutics. *Science* **297**, 353-356, doi:10.1126/science.1072994 (2002).

6 De Strooper, B., Vassar, R. & Golde, T. The secretases: enzymes with therapeutic potential in Alzheimer disease. *Nat Rev Neurol* **6**, 99-107, doi:10.1038/nrneurol.2009.218 (2010).

7 Jiang, L. *et al.* Structure-based discovery of fiber-binding compounds that reduce the cytotoxicity of amyloid beta. *Elife* **2**, e00857, doi:10.7554/eLife.00857 (2013).

8 Sevigny, J. *et al.* The antibody aducanumab reduces Abeta plaques in Alzheimer's disease. *Nature* **537**, 50-56, doi:10.1038/nature19323 (2016).

9 Howard, R. & Liu, K. Y. Questions EMERGE as Biogen claims aducanumab turnaround. *Nat Rev Neurol* **16**, 63-64, doi:10.1038/s41582-019-0295-9 (2020).

10 Morris, G. P., Clark, I. A. & Vissel, B. Questions concerning the role of amyloid-beta in the definition, aetiology and diagnosis of Alzheimer's disease. *Acta Neuropathol* **136**, 663-689, doi:10.1007/s00401-018-1918-8 (2018).

11 Sperling, R. A., Karlawish, J. & Johnson, K. A. Preclinical Alzheimer disease-the challenges ahead. *Nat Rev Neurol* **9**, 54-58, doi:10.1038/nrneurol.2012.241 (2013).

12 Voigt, F. F. *et al.* The mesoSPIM initiative: open-source light-sheet microscopes for imaging cleared tissue. *Nat Methods*, doi:10.1038/s41592-019-0554-0 (2019).

13 Herrmann, U. S. *et al.* Structure-based drug design identifies polythiophenes as antiprion compounds. *Sci Transl Med* **7**, 299ra123, doi:10.1126/scitranslmed.aab1923 (2015).

14 Margalith, I. *et al.* Polythiophenes inhibit prion propagation by stabilizing prion protein (PrP) aggregates. *J Biol Chem* **287**, 18872-18887, doi:10.1074/jbc.M112.355958 (2012).

15 Neumann, U. *et al.* A novel BACE inhibitor NB-360 shows a superior pharmacological profile and robust reduction of amyloid-beta and neuroinflammation in APP transgenic mice. *Molecular neurodegeneration* **10**, 44, doi:10.1186/s13024-015-0033-8 (2015).

16 Neumann, U., Machauer, R. & Shimshek, D. R. The beta-secretase (BACE) inhibitor NB-360 in preclinical models: From amyloid-beta reduction to downstream disease-relevant effects. *Br J Pharmacol*, doi:10.1111/bph.14582 (2019).

17 Paganetti, P. A., Lis, M., Klafki, H. W. & Staufenbiel, M. Amyloid precursor protein truncated at any of the gamma-secretase sites is not cleaved to beta-amyloid. *J Neurosci Res* **46**, 283-293, doi:10.1002/(SICI)1097-4547(19961101)46:3<283::AID-JNR1>3.0.CO;2-G (1996).

18 Radde, R. *et al.* Abeta42-driven cerebral amyloidosis in transgenic mice reveals early and robust pathology. *EMBO Rep* **7**, 940-946, doi:10.1038/sj.embor.7400784 (2006).

19 Pfeifer, M. *et al.* Cerebral hemorrhage after passive anti-Abeta immunotherapy. *Science* **298**, 1379, doi:10.1126/science.1078259 (2002).

20 Yang, B. *et al.* Single-Cell Phenotyping within Transparent Intact Tissue through Whole-Body Clearing. *Cell* **158**, 945-958, doi:10.1016/j.cell.2014.07.017 (2014).

21 Kirschenbaum, D. *Electrophoretic tissue clearing and staining chamber*, <https://grabcad.com/library/electrophoretic-tissue-clearing-and-staining-chamber-1> (2020).

22 Chung, K. *et al.* Structural and molecular interrogation of intact biological systems. *Nature* **497**, 332-337, doi:10.1038/nature12107

nature12107 [pii] (2013).

23 Nystrom, S. *et al.* Evidence for age-dependent in vivo conformational rearrangement within Abeta amyloid deposits. *ACS chemical biology* **8**, 1128-1133, doi:10.1021/cb4000376 (2013).
24 Bria, A. & Iannello, G. TeraStitcher - a tool for fast automatic 3D-stitching of teravoxel-sized microscopy images. *BMC Bioinformatics* **13**, 316, doi:10.1186/1471-2105-13-316 (2012).
25 Dadgar-Kiani, E. *Quantification....* <https://github.com/leelabhub/alz-drug-3d/> (2020).
26 Wang, Q. *et al.* The Allen Mouse Brain Common Coordinate Framework: A 3D Reference Atlas. *Cell* **181**, 936-953 e920, doi:10.1016/j.cell.2020.04.007 (2020).
27 Renier, N. *et al.* Mapping of Brain Activity by Automated Volume Analysis of Immediate Early Genes. *Cell* **165**, 1789-1802, doi:10.1016/j.cell.2016.05.007 (2016).
28 Berg, S. *et al.* ilastik: interactive machine learning for (bio)image analysis. *Nat Methods* **16**, 1226-1232, doi:10.1038/s41592-019-0582-9 (2019).
29 Benjamini, Y., Drai, D., Elmer, G., Kafkafi, N. & Golani, I. Controlling the false discovery rate in behavior genetics research. *Behav Brain Res* **125**, 279-284, doi:10.1016/s0166-4328(01)00297-2 (2001).
30 Ortiz, C. *et al.* Molecular atlas of the adult mouse brain. *Sci Adv* **6**, eabb3446, doi:10.1126/sciadv.abb3446 (2020).
31 Institute, A. *Allen Cell Types Database*, <https://portal.brain-map.org/atlases-and-data/rnaseq/mouse-whole-cortex-and-hippocampus-10x> (2015).
32 Bradski, G. The OpenCV library. *Dr Dobbs J* **25**, 120-+ (2000).
33 Furth, D. *et al.* An interactive framework for whole-brain maps at cellular resolution. *Nat Neurosci* **21**, 139-149, doi:10.1038/s41593-017-0027-7 (2018).
34 Klein, S., Staring, M., Murphy, K., Viergever, M. A. & Pluim, J. P. W. elastix: A Toolbox for Intensity-Based Medical Image Registration. *IEEE transactions on medical imaging* **29**, 196-205, doi:10.1109/Tmi.2009.2035616 (2010).
35 Millman, K. J. & Aivazis, M. Python for Scientists and Engineers. *Comput Sci Eng* **13**, 9-12, doi:Doi 10.1109/Mcse.2011.36 (2011).
36 Tomer, R., Ye, L., Hsueh, B. & Deisseroth, K. Advanced CLARITY for rapid and high-resolution imaging of intact tissues. *Nat Protoc* **9**, 1682-1697, doi:10.1038/nprot.2014.123 (2014).
37 Rasmussen, J. *et al.* Amyloid polymorphisms constitute distinct clouds of conformational variants in different etiological subtypes of Alzheimer's disease. *Proc Natl Acad Sci U S A* **114**, 13018-13023, doi:10.1073/pnas.1713215114 (2017).
38 Rijal Upadhaya, A. *et al.* Biochemical stages of amyloid-beta peptide aggregation and accumulation in the human brain and their association with symptomatic and pathologically preclinical Alzheimer's disease. *Brain* **137**, 887-903, doi:10.1093/brain/awt362 (2014).
39 Vieira, P. & Rajewsky, K. The half-lives of serum immunoglobulins in adult mice. *Eur J Immunol* **18**, 313-316, doi:10.1002/eji.1830180221 (1988).
40 Tarozzo, G. *et al.* Fractalkine protein localization and gene expression in mouse brain. *J Neurosci Res* **73**, 81-88, doi:10.1002/jnr.10645 (2003).
41 Richardson, D. S. & Lichtman, J. W. Clarifying Tissue Clearing. *Cell* **162**, 246-257, doi:10.1016/j.cell.2015.06.067 (2015).
42 Balakrishnan, K. *et al.* Impact of amyloid beta aggregate maturation on antibody treatment in APP23 mice. *Acta Neuropathol Commun* **3**, 41, doi:10.1186/s40478-015-0217-z (2015).
43 Jucker, M. & Walker, L. C. Self-propagation of pathogenic protein aggregates in neurodegenerative diseases. *Nature* **501**, 45-51, doi:10.1038/nature12481 (2013).
44 Burgold, S., Filser, S., Dorostkar, M. M., Schmidt, B. & Herms, J. In vivo imaging reveals sigmoidal growth kinetic of beta-amyloid plaques. *Acta Neuropathol Commun* **2**, 30, doi:10.1186/2051-5960-2-30 (2014).
45 Hellstrand, E., Boland, B., Walsh, D. M. & Linse, S. Amyloid beta-protein aggregation produces highly reproducible kinetic data and occurs by a two-phase process. *ACS Chem Neurosci* **1**, 13-18, doi:10.1021/cn900015v (2010).
46 Peters, F. *et al.* BACE1 inhibition more effectively suppresses initiation than progression of beta-amyloid pathology. *Acta Neuropathol* **135**, 695-710, doi:10.1007/s00401-017-1804-9 (2018).

47 Brendel, M. *et al.* Efficacy of chronic BACE1 inhibition in PS2APP mice depends on the regional A beta deposition rate and plaque burden at treatment initiation. *Theranostics* **8**, 4957-4968, doi:10.7150/thno.27868 (2018).

48 Cohen, S. I. *et al.* Proliferation of amyloid-beta42 aggregates occurs through a secondary nucleation mechanism. *Proc Natl Acad Sci U S A* **110**, 9758-9763, doi:10.1073/pnas.1218402110 (2013).

49 Szepesi, Z., Manouchehrian, O., Bachiller, S. & Deierborg, T. Bidirectional Microglia-Neuron Communication in Health and Disease. *Front Cell Neurosci* **12**, 323, doi:10.3389/fncel.2018.00323 (2018).

50 Chen, W. T. *et al.* Spatial Transcriptomics and In Situ Sequencing to Study Alzheimer's Disease. *Cell*, doi:10.1016/j.cell.2020.06.038 (2020).

51 Hu, X. *et al.* Bace1 modulates myelination in the central and peripheral nervous system. *Nat Neurosci* **9**, 1520-1525, doi:10.1038/nn1797 (2006).

52 Duncan, J. & Owen, A. M. Common regions of the human frontal lobe recruited by diverse cognitive demands. *Trends in neurosciences* **23**, 475-483, doi:10.1016/s0166-2236(00)01633-7 (2000).

Table 1. Plaque loads in control mice of each treatment cohort show low variability.

Treatment	Age	Count Mean	Count SD	Count SE
AB	old	2108735	292186	130670
AB	young	1097711	159214	79607
BACE1	old	2790290	245900	122950
BACE1	young	1151097	159849	79924
LCP	old	2738744	333892	166946
LCP	young	1243608	156807	64016
<all>	old	2512293	426799	118373
<all>	young	1175491	159340	42585

Table 2. Significantly affected voxels (SAV) after NB360, β1-antibody or LIN5044 treatment. After all the brain scans were registered to a brain atlas, the brains were deconstructed into standard voxels in a coordinate system. Then, for every treatment a "phantom" brain-volume was generated where each voxel represented the p-value of treatment effect. This was generated by two-sided t-testing all treated against all control brains (for a respective voxel). Voxels with p-values either p<0.1 or 0.05 were termed as SAV. Each treatment's phantom brain was thresholded to only contain SAVs (p<0.1 or 0.05). The effect-overlap between treatments was defined by the voxels which were significantly affected in both of the compared treatments. Our results show that most SAVs are non-overlapping. The overlap was <1% or <2.65% at p<0.05 or p<0.1, respectively.

p<0.05							
Young				Old			
Density	NB360	β1	LIN5044	Density	NB360	β1	LIN5044
NB360	2'649'191	435	2	NB360	46	0	0
β1	435	4'625	0	β1	0	40	0
LIN5044	2	0	29	LIN5044	0	0	276
Size	NB360	β1	LIN5044	Size	NB360	β1	LIN5044
NB360	66'128	3	1	NB360	10	0	0
β1	3	2'518	0	β1	0	18	1
LIN5044	1	0	80	LIN5044	0	1	492'779
Maturity	NB360	β1		Maturity	NB360	β1	
NB360	1'593'392	9'542		NB360	136	0	
β1	9'542	52'893		β1	0	639	
p<0.1							

Young				Old			
Density	NB360	β1	LIN5044	Density	NB360	β1	LIN5044
NB360	7’185’540	5’443	30	NB360	16304	0	0
β1	5’443	21’359	0	β1	0	69	0
LIN5044	30	0	121	LIN5044	0	0	486
Size	NB360	β1	LIN5044	Size	NB360	β1	LIN5044
NB360	888’437	282	1’302	NB360	25	0	0
β1	282	8’661	1	β1	0	61	5
LIN5044	1’302	1	20’530	LIN5044	0	5	2’941’884
Maturity	NB360	β1		Maturity	NB360	β1	
NB360	2’181’488	19’777		NB360	221	0	
β1	19’777	84’862		β1	0	1432	

Extended Data Figures and legends

Extended data figure 1. (a) Schematic of sample quantification pipeline describes the segmentation of plaques, registration of autofluorescence channel to an atlas, and finally application of the registration transformation to plaque information (location, maturity, size) to a generalized atlas space where group-level analysis can be performed. (b) The Receiver Operating Characteristic and Precision Recall curves quantify the accuracy of plaque detection on an expert-annotated test dataset - showing both very high precision and recall. (c) Pivotal steps in the data analysis pipeline include accurate registration of brains to a standard atlas and plaque segmentation with expert-trained machine learning. Whole mouse brain data were analyzed in a multi-step process. First, brains are registered to the Allen Brain Atlas through non-linear transformations. Brain regions (green outlines) match with the autofluorescence of the brain data well. (d) Plaque segmentation with expert-trained machine learning allows for automated segmentation of entire brains. (e) Machine learning based segmentation fits well with raw data. Plaques are spherical as captured with a camera orthogonal to the light-sheet illumination (c, Orthogonal imaging plane), but show spindle artefacts when digitally resliced orthogonally (c, Orthogonal reslice - Raw), due to an elongated axial point-spread function of the microscope. Segmentation with expert-trained machine learning decreased spindle artefacts (c, Orthogonal reslice – Raw and Segmented). Segmented plaques in atlas-registered brains (f; left) are voxelized resulting in heatmaps of either plaque density, mean size or maturity (f; right), which can be used for downstream voxel-based statistics. (g) Alternatively, statistics on segmented plaques can be done by grouping them into brain regions.

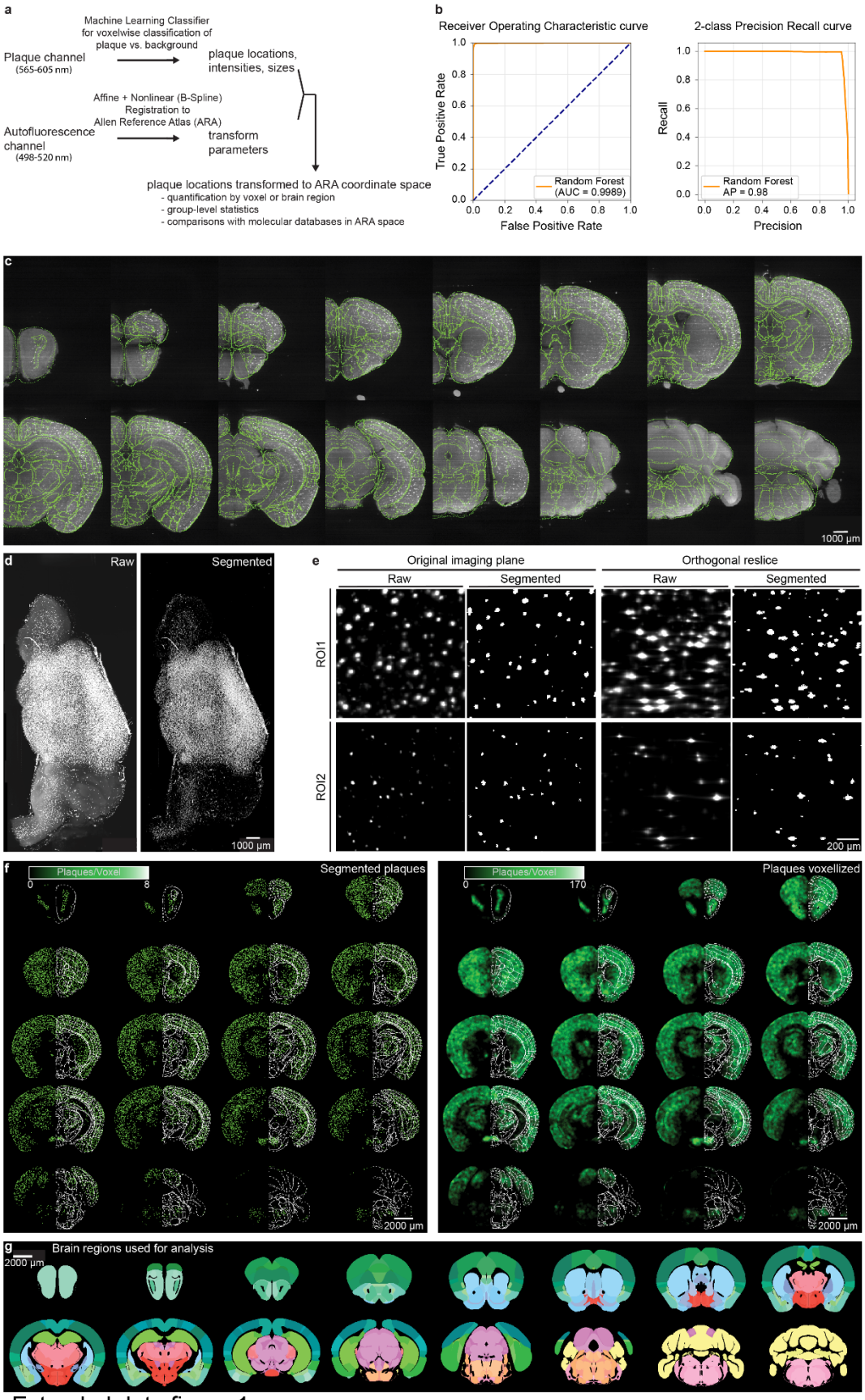

Extended data figure 1

Extended data figure 2. Custom-made data analysis pipeline handles raw image data automatically and results in intuitive heatmaps of treatment effect. (**a**) Statistical pipeline of whole-brain analysis starting from stitched whole-brain mesoSPIM images and resulting in maps of significantly affected voxels (SAVs) in the end. Stitched whole-brain images were transformed and registered to a standard brain atlas, followed by voxellation of the registered volumes. (**b**) Descriptive statistics were calculated for every voxel of individual brains resulting in plaque counts, mean plaque size and mean intensity ratio for each voxel (plaques: P1, P2 … Pn). Intensity ratios were calculated by dividing the peak fluorescent emission in the qFTAA channel with the peak emission of the hFTAA channel in the center of each plaque. (**c**) Descriptive statistics for each treatment and control cohort were calculated by calculating mean values of corresponding voxels across individual brains within a cohort. (**d**) Inferential statistical tests to compare treated and control cohorts were applied on cohort-level statistics across each voxel. Significantly affected voxels were mapped on digitally resliced coronal brain sections (p-map).

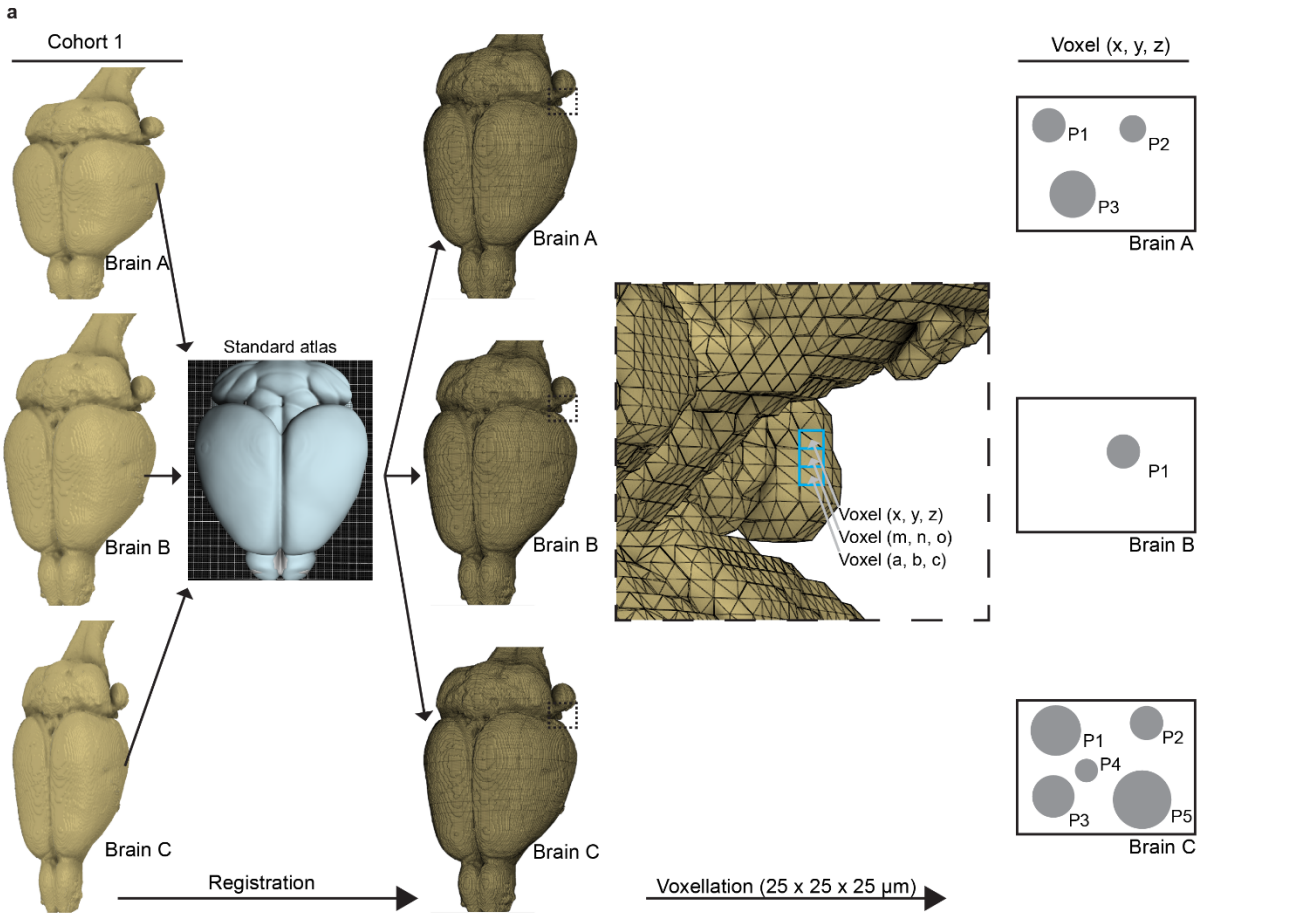

b

Descriptive statistics of a voxel.

Voxel (x, y, z)	Plaque count	Mean plaque size	Mean intensity ratio
Brain A: P1, P2, P3	$3 = D_A$	$\frac{V_{P1}+V_{P2}+V_{P3}}{3} = S_A$	$\frac{I_{498nm}}{I_{565nm}} = R$ (qFTAA / hFTAA) $\frac{R_{P1}+R_{P2}+R_{P3}}{3} = R_A$
Brain B: P1	$1 = D_B$	$\frac{V_{P1}}{1} = S_B$	$\frac{R_{P1}}{1} = R_B$
Brain C: P1, P2, P3, P4, P5	$5 = D_C$	$\frac{V_{P1}+ \dots +V_{P5}}{5} = S_C$	$\frac{R_{P1}+ \dots +R_{P5}}{5} = R_C$

c

Descriptive statistics of a voxel in a cohort of samples.

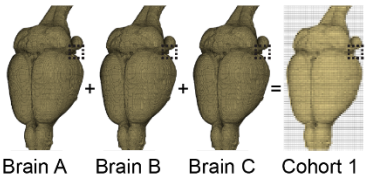

	Density	Size	Intensity ratio
$Cohort\ 1_{Voxel\ (x, y, z)}$	$\frac{D_A+D_B+D_C}{3}$	$\frac{S_A+S_B+S_C}{3}$	$\frac{R_A+R_B+R_C}{3}$

d

Comparison of two sample cohorts based on inferential statistics of all voxels across all samples.

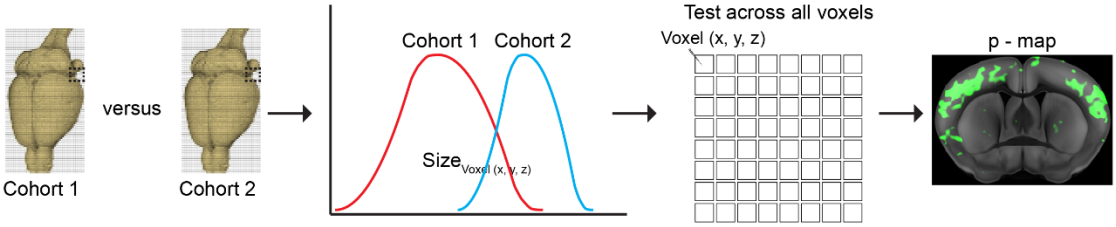

Extended data figure 2

Extended data figure 3. The β1 antibody treatment shows a limited effect across all analyzed metrics. (**a**) The β1 antibody treatment showed very limited effects in all analyzed brain regions across all analyzed metrics (**b**) There was a trend of reduction in the mean frequency of small plaques, but there was no change in plaque maturity.

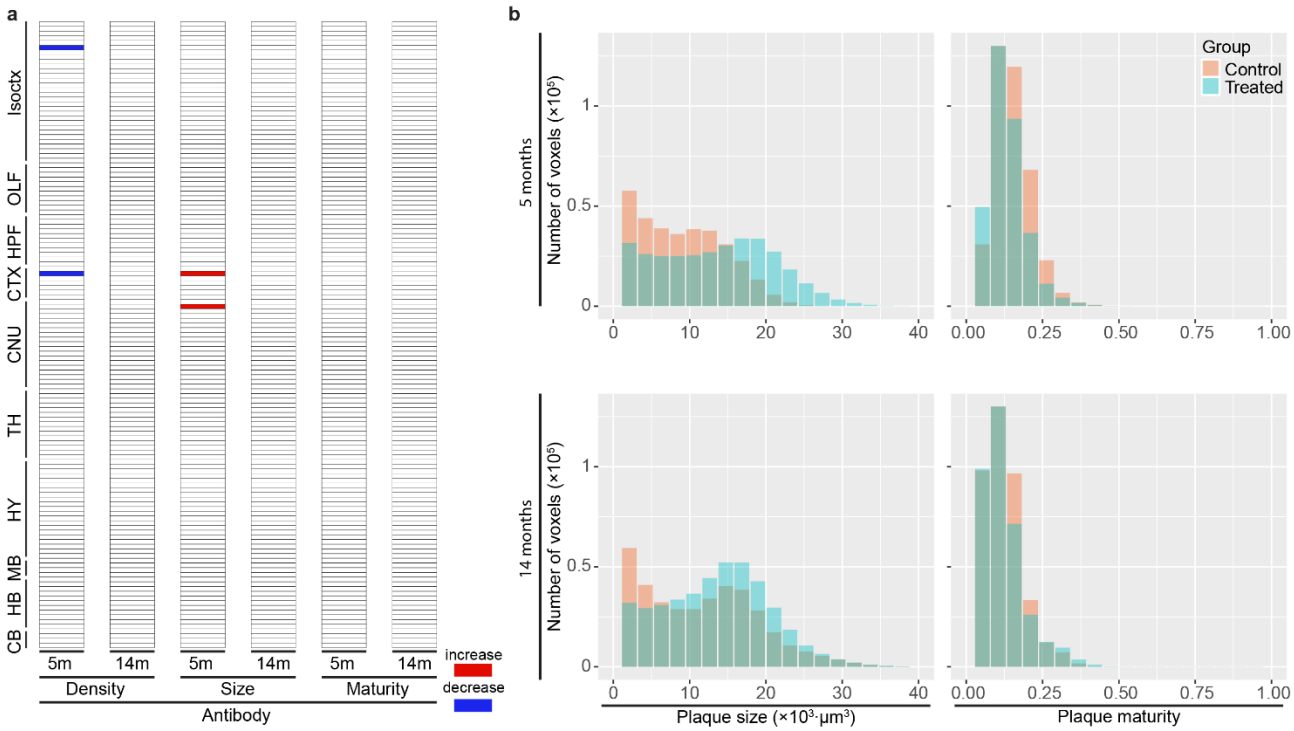

Extended data figure 3

Extended data figure 4. Plaque count reduction by β1 antibody is minimal in 5-month-old mice and absent in old mice. (**a**) SAV upon β1 antibody treatment. Significant effects occurred mostly in the brainstem. (**b**) Plaque count reduction in the 40 brain regions with the most significant therapy-induced changes (0.0139<p< 0.4658) in the left hemisphere. (**c**) Heatmaps of regional plaque burden in individual mice in 5-mont-old mice. (**d**) The plaque-count change induced by β1 antibody treatment in 14-month-old mice is negligible on the voxel level. (**e**) Fold-change reduction of plaque count of the 40 brain regions with the most significant therapy-induced changes (0.3284<p< 0.4835) in the left hemisphere at 14-months. (**f**) Heatmaps of regional plaque burden in individual mice in 5-mont-old mice. Isoctx – isocortex, OLF – olfactory areas, HPF – hippocampal formation, CTX sp – cortical subplate, CNU – caudate nucleus, TH – thalamus, HY – hypothalamus, MB – midbrain, HB – hindbrain, CB – cerebellum.

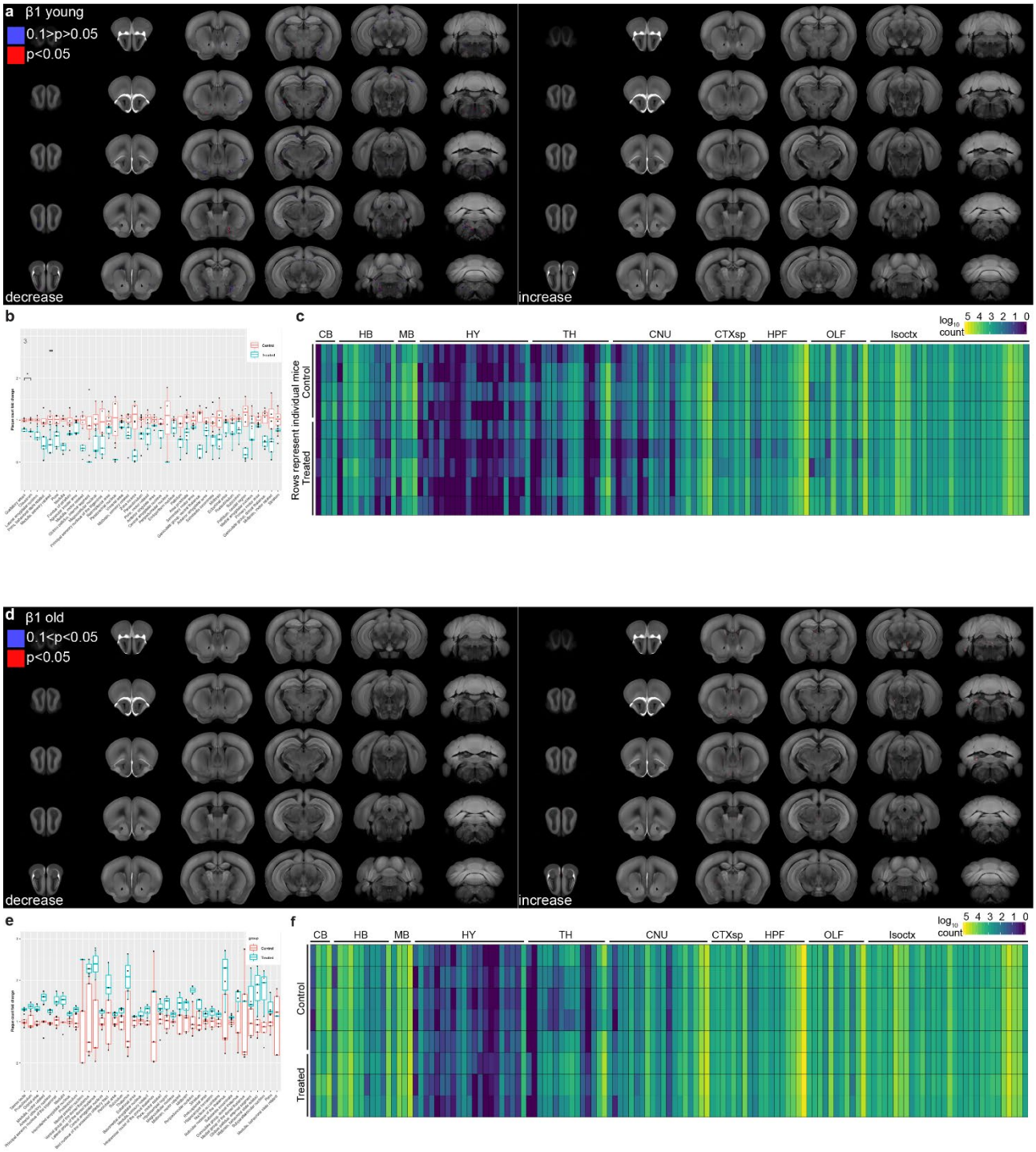

Extended data figure 4

Extended data figure 5. BACE1-inhibition induced conspicuous plaque count reduction in 5-month-old mice, but not in 14-month-old mice. (**a**) Heatmap of voxels with significant plaque count reduction upon NB360 treatment in young mice, compared to control. (**b**) Fold-change reduction of plaque count of the 40 brain regions with the most significant therapy-induced changes ($0.0043<p<0.0091$) in the left hemisphere. (**c**) Heatmap of regional plaque burden in individual mice. The strong effect of BACE1 inhibition is conspicuous on the single-sample level. (**d**) Upon BACE1 inhibition in 14-month-old mice only very few voxels show significant plaque-count reduction. (**e**) Fold-change reduction of plaque count of the 40 brain regions with the most significant therapy-induced changes ($0.0159<p<0.1338$) in the left hemisphere at 14-months. (**f**) Heat map of regional plaque burden in individual mice at 14-months of age. Isoctx – isocortex, OLF – olfactory areas, HPF – hippocampal formation, CTX sp – cortical subplate, CNU – caudate nucleus, TH – thalamus, HY – hypothalamus, MB – midbrain, HB – hindbrain, CB – cerebellum

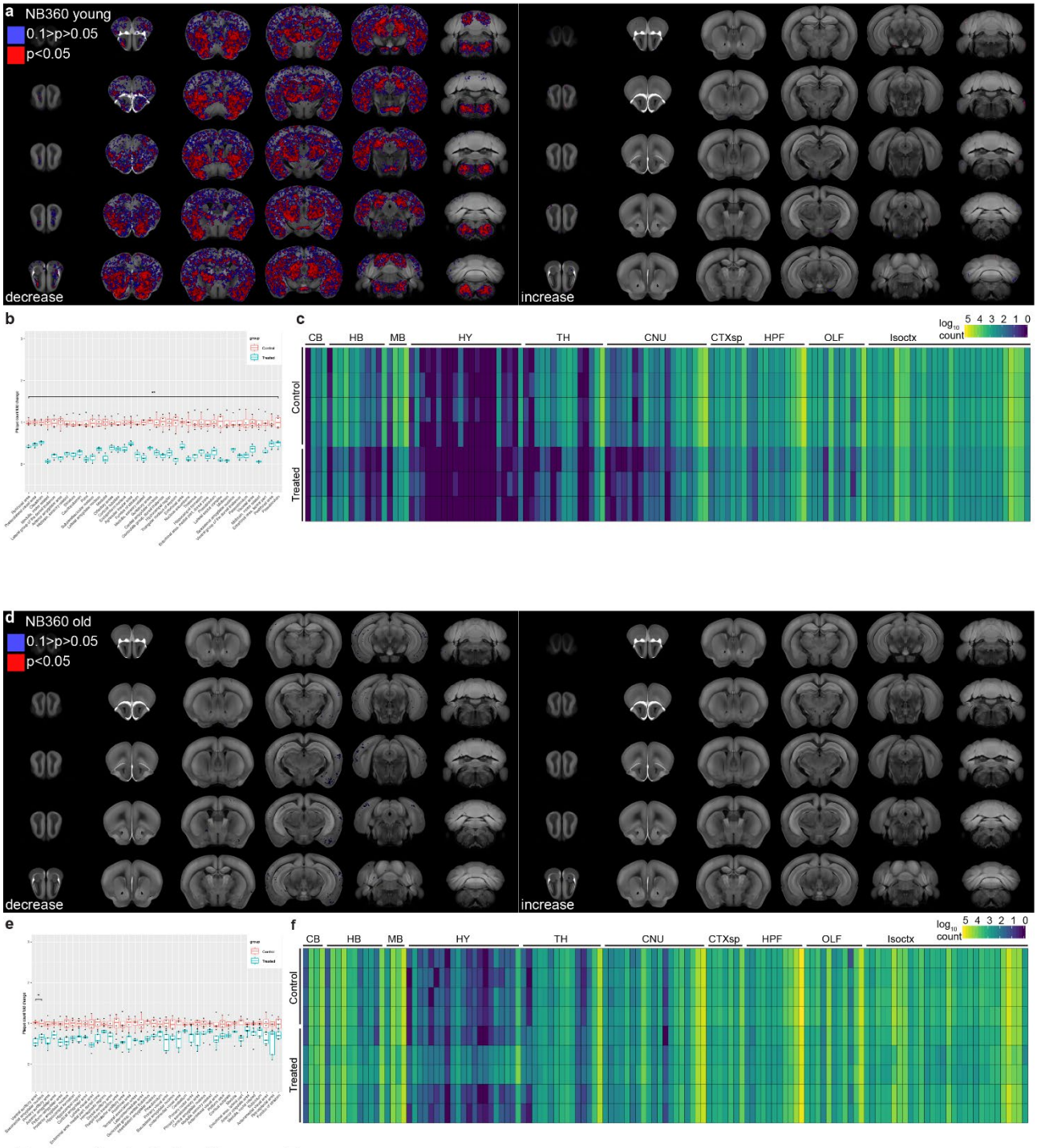

Extended data figure 5

Extended data figure 6. BACE1-inhibition induces considerable plaque size reduction in 5-month-old mice, but not in 14-month-old mice. (**a**) Heatmap of voxels with significant mean plaque size reduction upon NB360 treatment in young mice, compared to control. (**b**) Fold-change reduction of mean plaque size of the 40 brain regions with the most significant therapy-induced changes ($0.0236<p<0.0425$) in the left hemisphere. (**c**) Heatmap of regional mean plaque sizes in individual mice. (**d**) Heatmaps of significantly affected voxels show very limited plaque size change by BACE1-inhibition in 14-month-old mice. (**e**) Fold-change reduction of mean plaque size of the 40 brain regions with the most significant therapy-induced changes ($0.7641<p< 0.7641$) in the left hemisphere at 14-months. (**f**) Heatmap of regional mean plaque sizes in individual mice at 14-months of age. Isoctx – isocortex, OLF – olfactory areas, HPF – hippocampal formation, CTX sp – cortical subplate, CNU – caudate nucleus, TH – thalamus, HY – hypothalamus, MB – midbrain, HB – hindbrain, CB – cerebellum

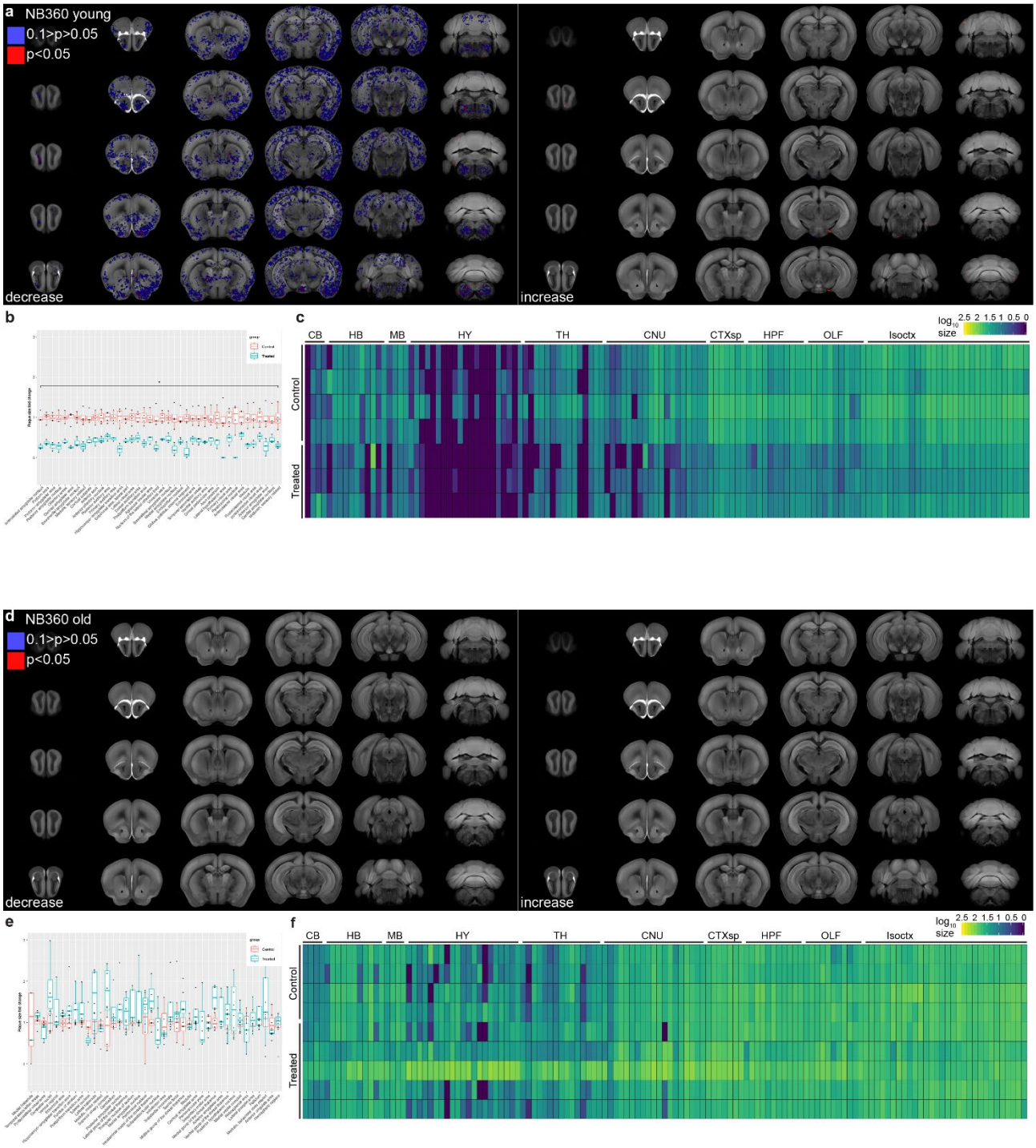

Extended data figure 6

Extended data figure 7. Trend in plaque-count reduction in few anatomical regions after LIN5044 treatment in 5- and 14-month-old mice. (**a**) Heatmap of voxels with significant plaque count reduction upon LIN5044 treatment, compared to control at 5-months of age. (**b**) Fold-change reduction of plaque count of the 40 brain regions with the most significant therapy-induced changes ($0.3022<p<0.8724$) in the left hemisphere. (**c**) Heatmap of regional plaque burden in individual mice. (**d**) Plaque-count reduction is not significant but shows a trend after LIN5044 treatment in 14-month-old mice. Heatmap of voxels with significant plaque count reduction upon LIN5044 treatment, compared to control. (**e**) Fold-change reduction of plaque count of the 40 brain regions with the most significant therapy-induced changes ($0.0913<p<0.6366$) in the left hemisphere in 14-months-old mice. (**f**) Heatmap of regional plaque burden in individual mice at 14-months of age. Isoctx – isocortex, OLF – olfactory areas, HPF – hippocampal formation, CTX sp – cortical subplate, CNU – caudate nucleus, TH – thalamus, HY – hypothalamus, MB – midbrain, HB – hindbrain, CB - cerebellum

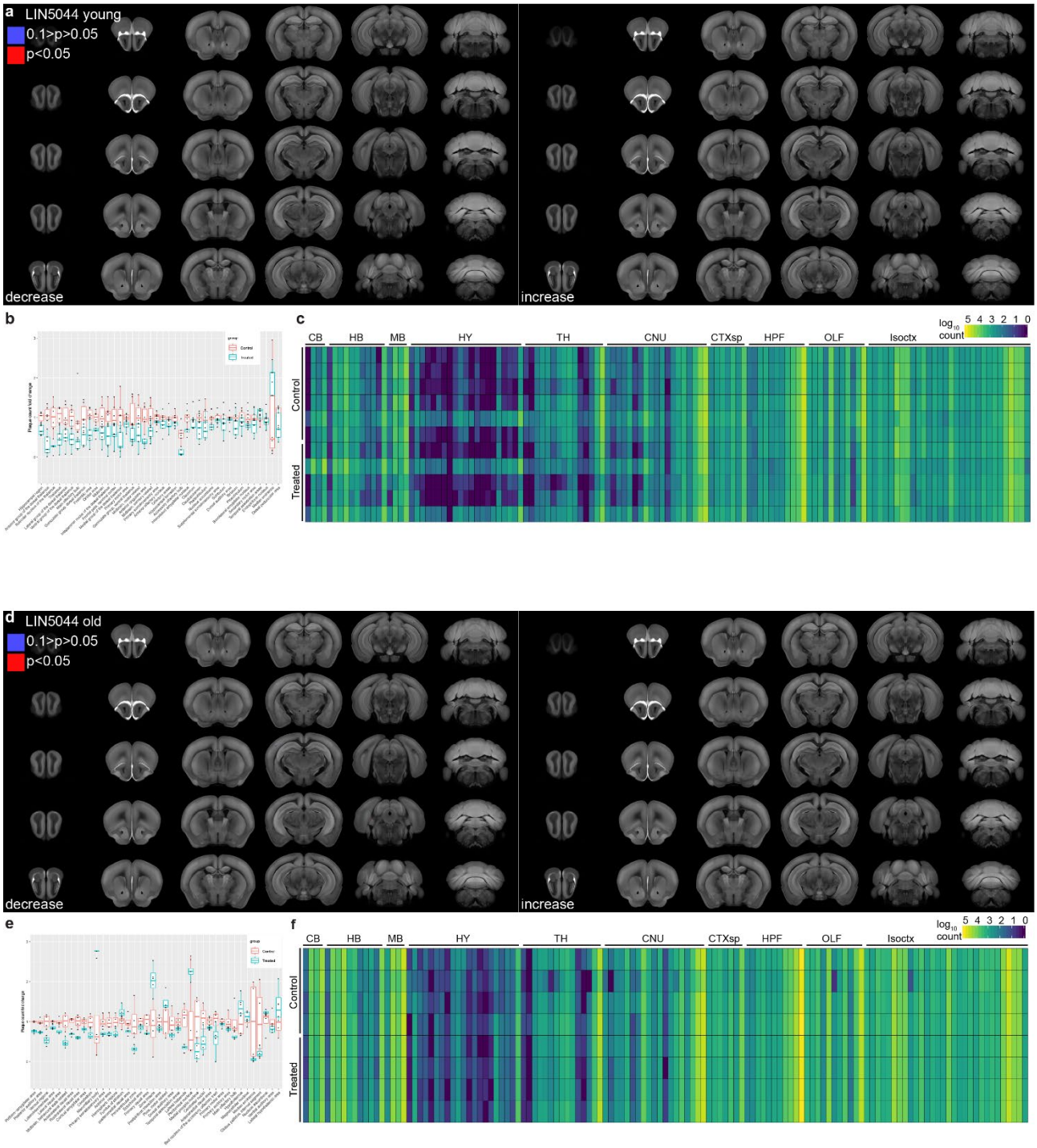

Extended data figure 7

Extended data figure 8. Mean plaque-sizes are significantly reduced in some anatomical regions after LIN5044 treatment in 5- and 14-month-old mice. (**a**) Heatmap of voxels with significant mean plaque size reduction upon LIN5044 treatment, compared to control. Cortical areas show some significant treatment effect. (**b**) Fold-change reduction of mean plaque size of the 40 brain regions with the most significant therapy-induced changes ($0.0197<p<0.1333$) in the left hemisphere. (**c**) Heatmap of regional mean plaque sizes in individual mice at 5-months. (**d**) Mean plaque-sizes after LIN5044 treatment in 14-month-old mice are significantly reduced with an emphasis in cortical areas. Heatmap of voxels with significant mean plaque size reduction upon LIN5044 treatment, compared to control at 14-months. (e) Fold-change reduction of mean plaque size of the 40 brain regions with the most significant therapy-induced changes ($0.0048<p<0.0865$) in the left hemisphere. (**f**) Heatmap of regional mean plaque sizes in individual mice at 14-months. The strong effect of LIN5044 is conspicuous on the single-sample level. Isoctx – isocortex, OLF – olfactory areas, HPF – hippocampal formation, CTX sp – cortical subplate, CNU – caudate nucleus, TH – thalamus, HY – hypothalamus, MB – midbrain, HB – hindbrain, CB - cerebellum

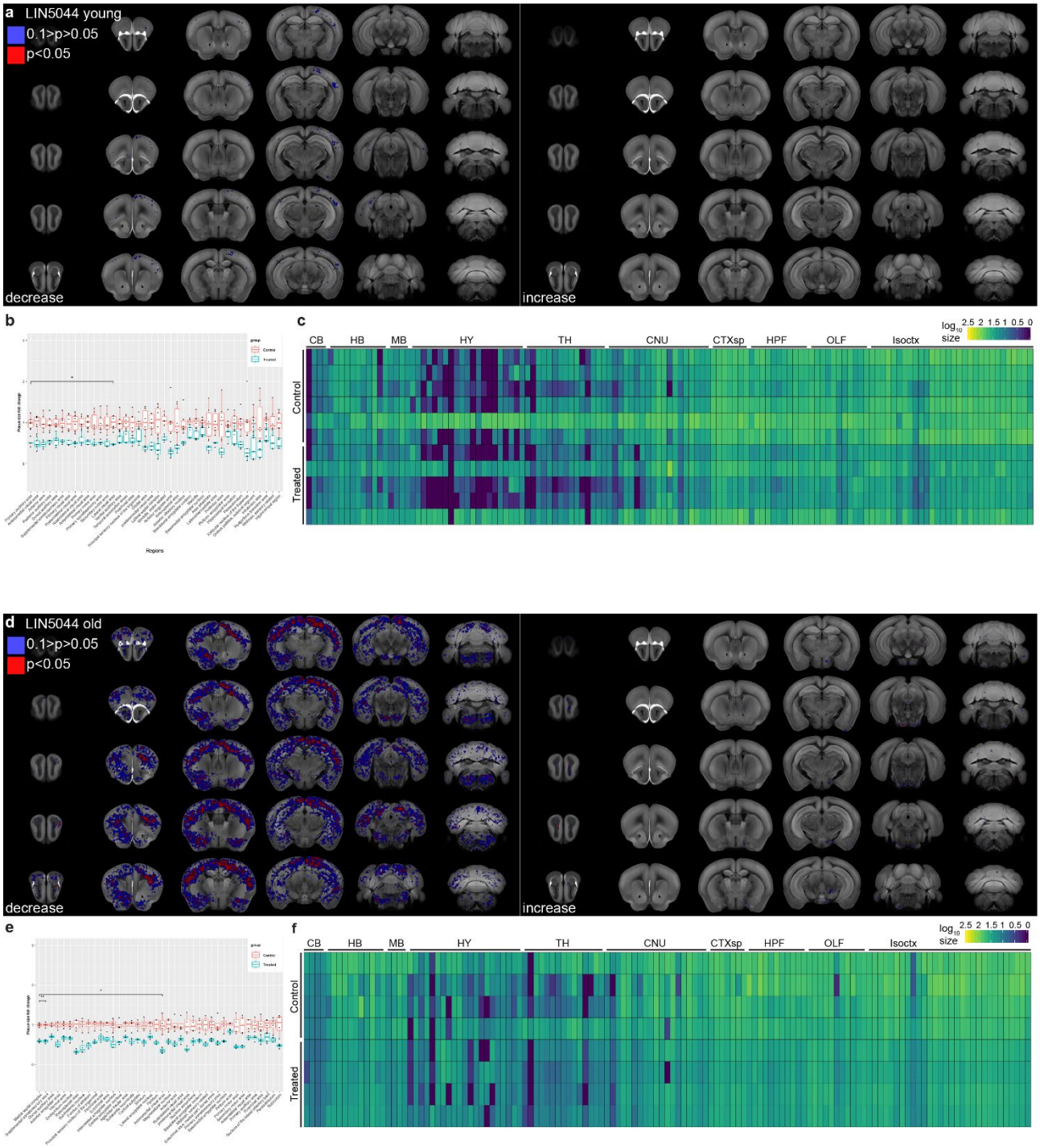

Extended data figure 8

Extended data figure 9. Anti-amyloid β treatments reduce plaque counts and sizes. (**a**) We randomly picked an optical slice from the cortex (**b**, ROI1, ROI2 white inserts) of a control and a treated brain in each treatment cohort. Next, we segmented the plaques and color-coded them such that colors represent 4 equal portions of the total range of plaque sizes. (**c**) NB360 conspicuously reduced numbers and sizes of plaques in young mice, while (**d**) LIN5044 the number of large plaques in aged mice. The effect in the other treatment cohorts is less obvious. (**e**) Voxel-based and anatomy-based plaque burden analysis differ in how the brain is spatially sampled for statistics. Voxel level statistics is more granular and highlights how treatment effects distribute in space in an unbiased way. We overlaid the outlines of anatomical brain regions on the voxel-based significance maps of therapy-affected voxels. Voxel-based statistics shows clusters of therapy-affected voxels occupying spaces which do not follow the boundaries of anatomical regions.

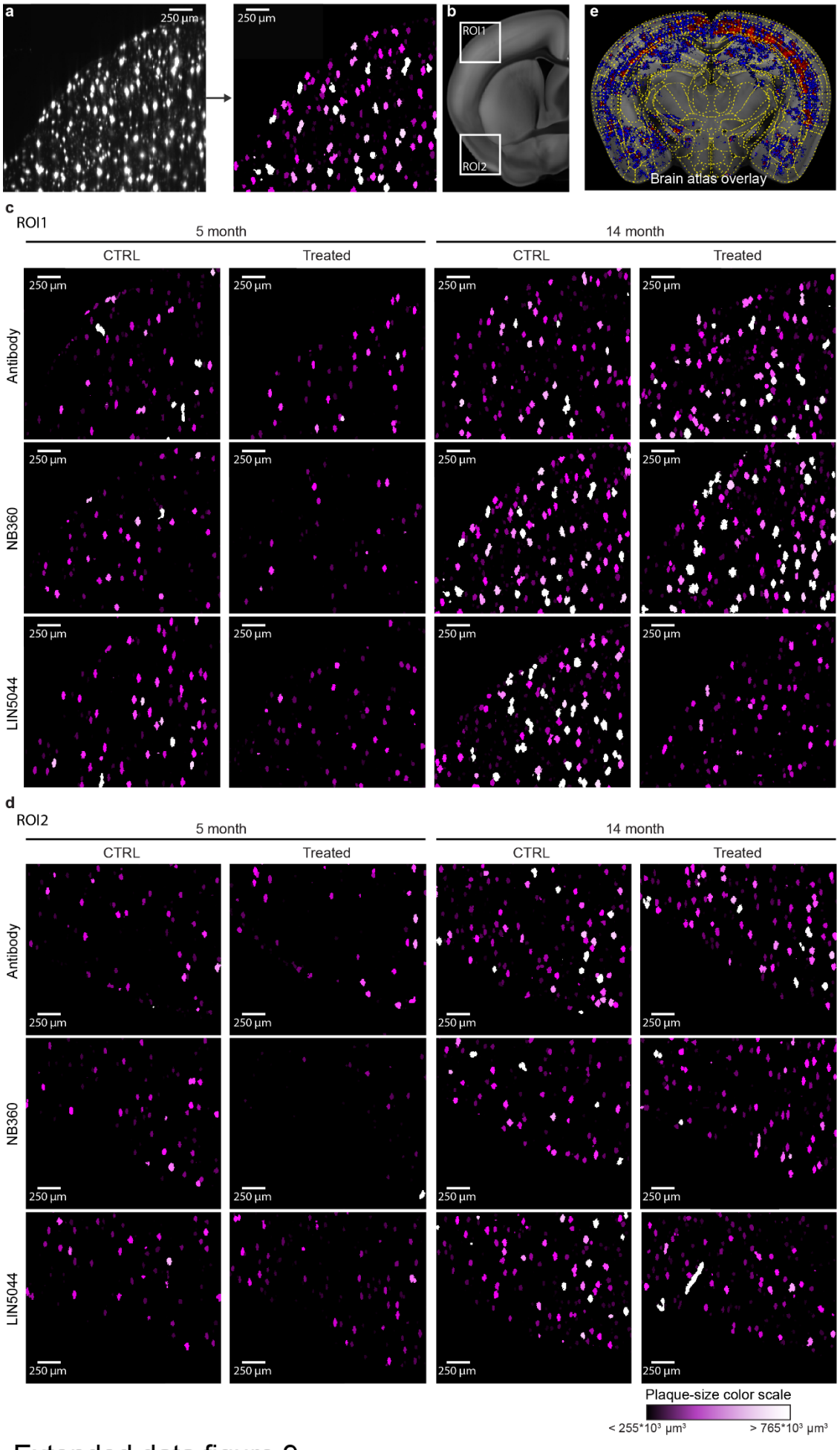

Extended data figure 9

Extended data figure 10. Regional variations of bioavailability do not explain the spatial patterns of drug effectiveness. (**a**) Brains were dissected into eight regions to test regional drug distributions. (**b**) No regional difference in NB360 drug levels detectable after oral administration, (**c**) while LIN5044 shows significantly higher levels in the brainstem (ranging $0.0023<p<0.0345$) and the cerebellum ($p = 0.0241$) 2 hours after intraperitoneal injection, (**d**) but no difference detectable at 6 hours. (**e, f**) ELISA measurements of β1 antibody levels after intraperitoneal application showed higher levels in the brainstem (for multiple brain regions ranging $p = 0.0223$ to $p<9\times10^{-4}$ at 6 hours and $p<10^{-4}$ at 24 hours) and the cerebellum (for multiple brain regions ranging $0.0072<p<0.034$ at 24 hours) compared to other regions both at 6 and 24 hours-similarly to LIN5044. (**g**) Pooled non-specific recombinant IgG shows no difference in regional distribution.

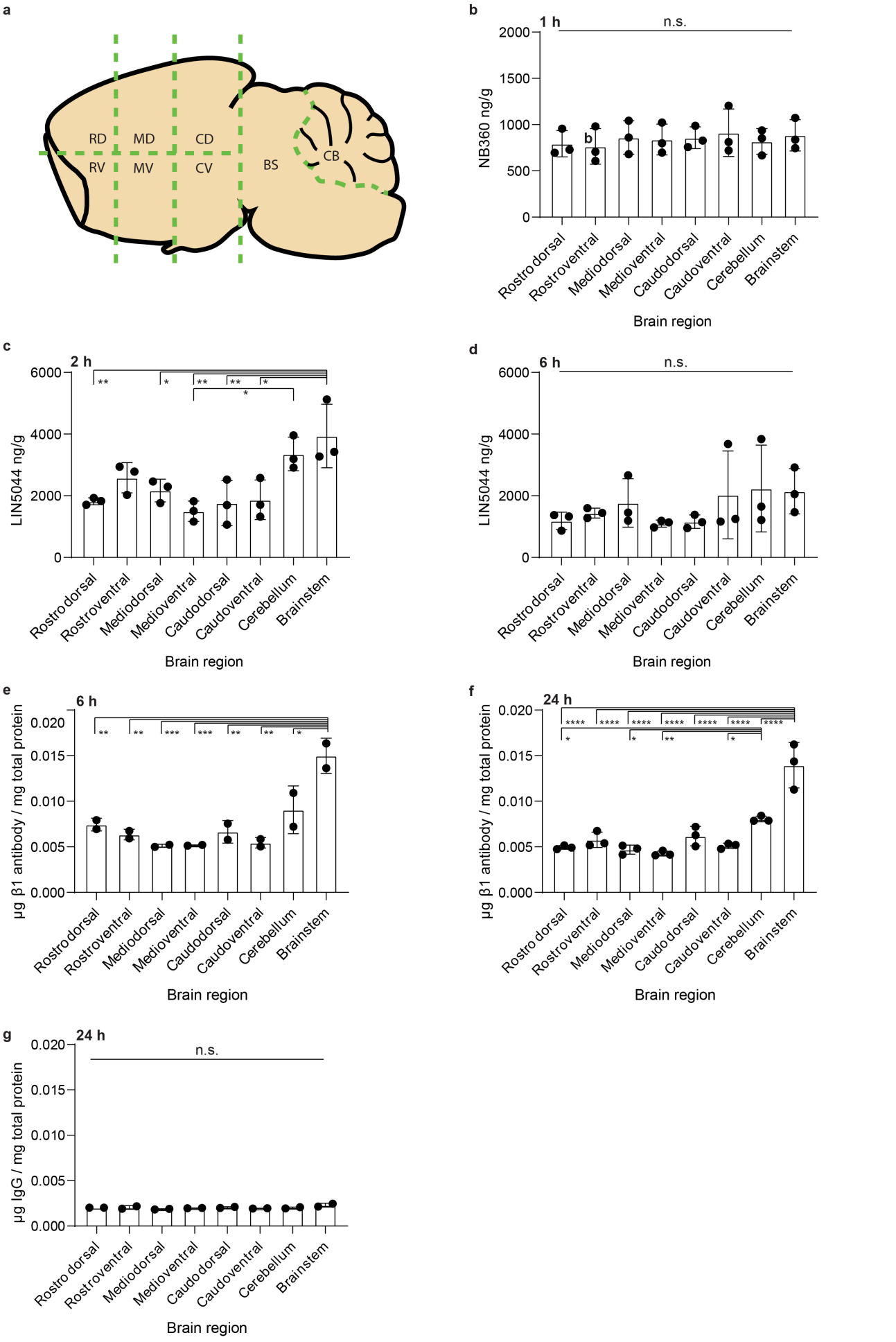

Extended data figure 10